MASTERARBEIT | MASTER'S THESIS

Titel | Title

Reservoir Properties of the Raminger Dolomite

verfasst von | submitted by

Richard William Scholey BSc

angestrebter akademischer Grad | in partial fulfilment of the requirements for the degree of

Master of Science (MSc)

Wien | Vienna, 2025

Studienkennzahl lt. Studienblatt | Degree programme code as it appears on the student record sheet:	UA 066 815
Studienrichtung lt. Studienblatt | Degree programme as it appears on the student record sheet:	Masterstudium Erdwissenschaften
Betreut von | Supervisor:	Dr. Kurt Decker

Contents

1 Abstract

This thesis characterizes the reservoir properties of Middle Triassic dolostomite to evaluate its potential for deep geothermal use, dolomites belong to the Raming Formation of the Göller Nappe exposed on the Hoher Lindkogel near Baden. The analysed outcrops are regarded analogues of hydrothermal reservoirs in the adjacent Vienna Basin.

Field investigations included bed-by-bed profiles and fracture density assessment by applying a fracture density classification, constant-head mini slug tests for in-situ permeability measurements, and the collection of samples for laboratory porosity and gas permeability testing. Results show a highly fractured carbonate unit with a reconstructed thickness of approximately 510 meters. Matrix permeability followed a log-normal trend with a mean value of 0.6 mD. Average porosity was determined to be at 1.46%. Both porosity and permeability were also found to increase with the fracture density. Permeability / porosity was found to increase from 0.1 mD / 0.6% (median values) in widely fractured dolomite to 0.13 mD / 1.1% in closely fractured and 1.1 mD / 1.2% in very closely fractured rock. When comparing the permeability / porosity values from gas permeability measurements is was found that both values decrease significantly with increasing confining pressures. The loss of permeability is up to more than 90% for confining pressures corresponding to about 3-3.5 km depth (6500 psi), porosity is reduced by 85%.

The distribution curves for the slug test permeability were used to conduct a Monte-Carlo simulation to determine possible production rates for the 500 m thick formation assuming different drawdown levels. A drawdown of 300 meters resulted in a 50% chance of gaining a flow rate of 300.000 litres of water per day which is approximately 3.5 litres per second and a drawdown of 100 m resulted a 50% chance of gaining a flow rate of 100.000 litres of water per day (1.2 litres per second). Both scenarios are insufficient for driving a district heating network which requires upwards of 50 litres per second. It should be noted that this study only dealt with the matrix properties of the dolomite neglecting the possible flow contribution by larger fractures or faults.

2 Abstract Deutsch

Diese Arbeit charakterisiert die Reservoireigenschaften von Dolomit aus der Mitteltrias, um dessen Potenzial für die tiefe Geothermie zu bewerten. Die Dolomite gehören zur Raming-Formation der Göller-Decke am Hohen Lindkogel bei Baden. Die analysierten Aufschlüsse gelten als Analoga zu hydrothermalen Aquiferen im angrenzenden Wiener Becken.

Die Felduntersuchungen umfassten die Aufnahme von Schichtprofilen mit der Bewertung der Kluftdichte, die in einem Klassifikationsschema erfasst wurde, Mini-Slug-Tests mit konstanter Druckhöhe für In-situ-Permeabilitätsmessungen und die Entnahme von Proben für Labormessungen der Porosität und Gasdurchlässigkeit. Die Ergebnisse zeigen eine stark geklüftete Karbonateinheit mit einer rekonstruierten Mächtigkeit von etwa 510 Metern. Die Matrixpermeabilität folgte einer logarithmischen Normalverteilung mit einem Mittelwert von 0,6 mD. Die durchschnittliche Porosität wurde mit 1,46 % ermittelt. Außerdem wurde festgestellt, dass sowohl Porosität als auch Permeabilität mit der Kluftdichte zunehmen. Die Permeabilität / Porosität nahm von 0,1 mD / 0,6 % (Medianwerte) in weit geklüftetem Dolomit auf 0,13 mD / 1,1 % in eng geklüftetem und 1,1 mD / 1,2 % in sehr eng geklüftetem Gestein zu. Beim Vergleich der Permeabilitäts-/Porositätswerte aus Gasdurchlässigkeitsmessungen wurde festgestellt, dass beide Werte mit zunehmendem Umgebungsdruck deutlich abnehmen. Der Permeabilitätsverlust beträgt mehr als 90 % bei Umgebungsdrücken, die einer Tiefe von etwa 3–3,5 km (6500 psi) entsprechen, die Porosität verringert sich um 85 %.

Die Verteilungskurven der Slug-Test-Permeabilität wurden für eine Monte-Carlo-Simulation verwendet, um die möglichen Produktionsraten für die 500 m mächtige Formation unter Annahme unterschiedlicher hydraulischer Absenkungsgrade zu bestimmen. Bei einer Absenkung von 300 Metern ergab sich eine 50-prozentige Wahrscheinlichkeit auf eine Durchflussrate von 300.000 Litern Wasser pro Tag (ca. 3,5 Liter pro Sekunde). Bei einer Absenkung von 100 Metern ergab sich eine 50-prozentige Chance auf eine Durchflussrate von 100.000 Litern Wasser pro Tag (ca. 1,2 Liter pro Sekunde). Beide Szenarien reichen nicht aus, um ein Fernwärmenetz zu betreiben, das eine Produktionsrate von mehr als 50 Liter pro Sekunde benötigt. Es ist zu beachten, dass sich diese Studie nur mit den Matrixeigenschaften des Dolomits befasste und den möglichen Beitrag größerer Brüche oder Störungen zur Durchlässigkeit der Formation vernachlässigte.

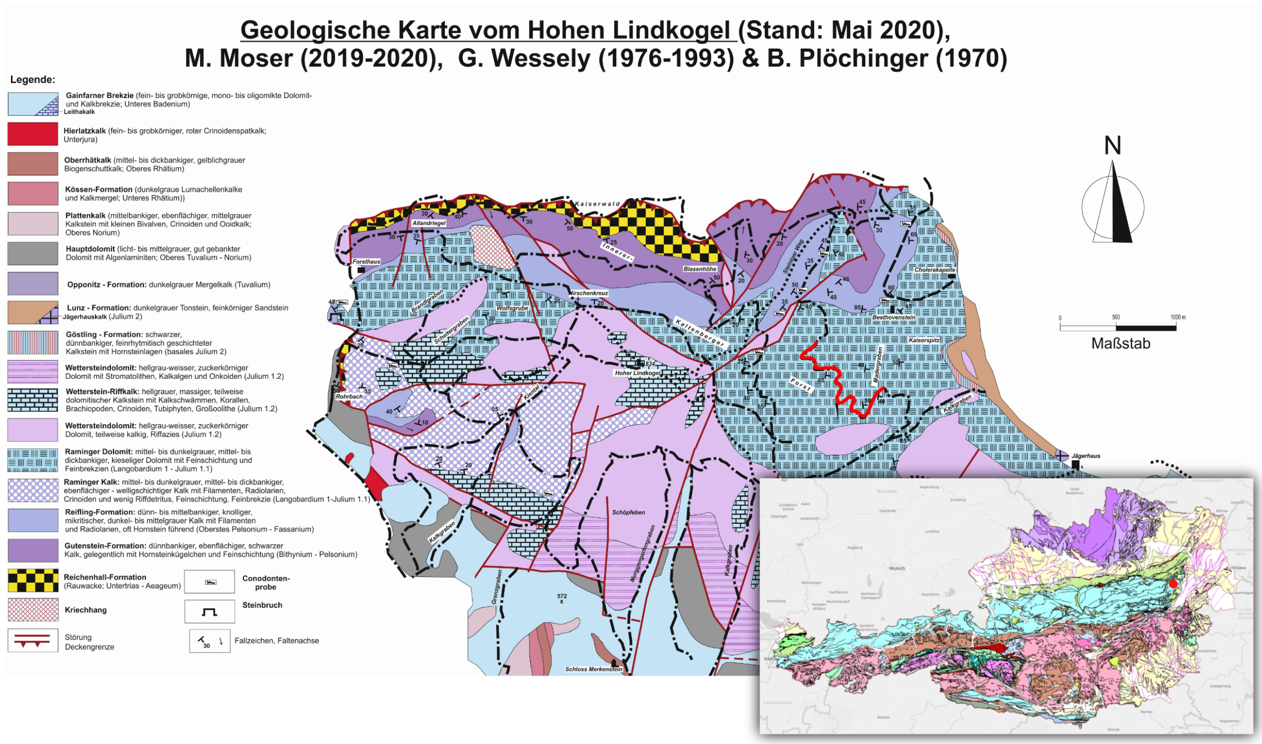

Figure 1: Forest road where measurements are taken shown in red [Moser, 2023]. Inset: Location of the Hohe Lindkogel within the NCA (Geosphere Maps 2025)

3 Introduction

One of the crucial prerequisites for the geothermal utilization of deep groundwater is the hydrogeological suitability of reservoir rocks to be exploited by geothermal doublets or triplets. This suitability is critical because it directly determines the economic viability of a geothermal project; without sufficient permeability and flow rates, a project cannot achieve the necessary heat extraction to generate electricity or provide district heating. In the deep subsurface of the southern Vienna Basin (Schwechat Deep, Tattendorf, Wiener Neustädter Deep), the large volumes of fractured carbonate rocks, part of the eastern extension of the limestone Alps and the Semmering System beneath the Miocene basin fill, are potential exploration targets. For a geothermal power plant to be viable in this region, target flow rates typically range from 50 to over 100 liters per second per production well. The focus of this study is on the Middle Triassic limestones and dolomites of the Wetterstein/Raminger Formation in the Göller Nappe, with the aim of assessing their potential to deliver the required productivity for both production and injection wells.

3.1 Goals

This master's thesis aims to characterize the reservoir properties of these potential groundwater storage units concerning their thickness, porosity, permeability, and fracture characteristics occurring in the rocks. To determine suitability for geothermal use, the following criteria for the Wetterstein/Raminger Dolomite of the Göller Nappe and Schneeberg Nappe are comparatively analysed to potentially establish a ranking of the units for geothermal use.

- **Fracture Distribution:** Distribution of Fracture Density Class (FDC) across available outcrops of the dolomite were determined in the field by measuring the fracture density on the outcrop surface.

- **Determination of basic hydrogeological parameters:** Porosity and permeability measurements in the laboratory and permeability measurements in outcrops.

The analyses are conducted in outcrops at the southwestern edge of the Vienna Basin, chosen to be stratigraphically and tectonically representative of the rocks in the Vienna Basin's subsurface. This thesis will test the hypothesis that the suitability of the Wetterstein series as a reservoir rock for deep geothermal use is independent of the nappe series order (Göller Nappe).

3.2 Work Program

- Literature review and identification/selection of suitable outcrops (sequence, fault zones).

- Development of a hypothetical reservoir concept based on Step 1.

- Fieldwork: Geological mapping, collection of rock samples for laboratory analysis, permeability measurements, fault surface analyses at outcrops. Primary collection points for samples and data for cross sections will be on the Lindkogel (Göller nappe, Fig. 1).

- Adjustment of the a-priori concept based on additional data and cartographic work:
  - Creation of reservoir profiles (conceptual vertical sections) and hydraulic assessment of fault zones.
  - Conclusions regarding the research hypotheses.

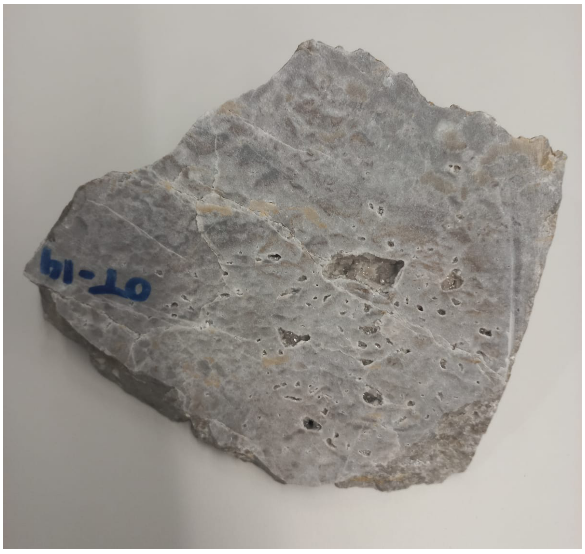

Figure 2: Example Raminger Dolomite collected from Ottersböck Quarry

3.2.1 Location

The location chosen is that of the Hohe Lindkogel in Baden (Fig. 1). Initial exploration of it and its surrounding areas revealed it to be the only suitable location to conduct the multitude of tests required to adequately determine the reservoir properties of these dolomites. Fig. 1. details the stretch of forest road that shall be analysed as these outcrops are well visible along this road allowing ease of access with all the necessary equipment.

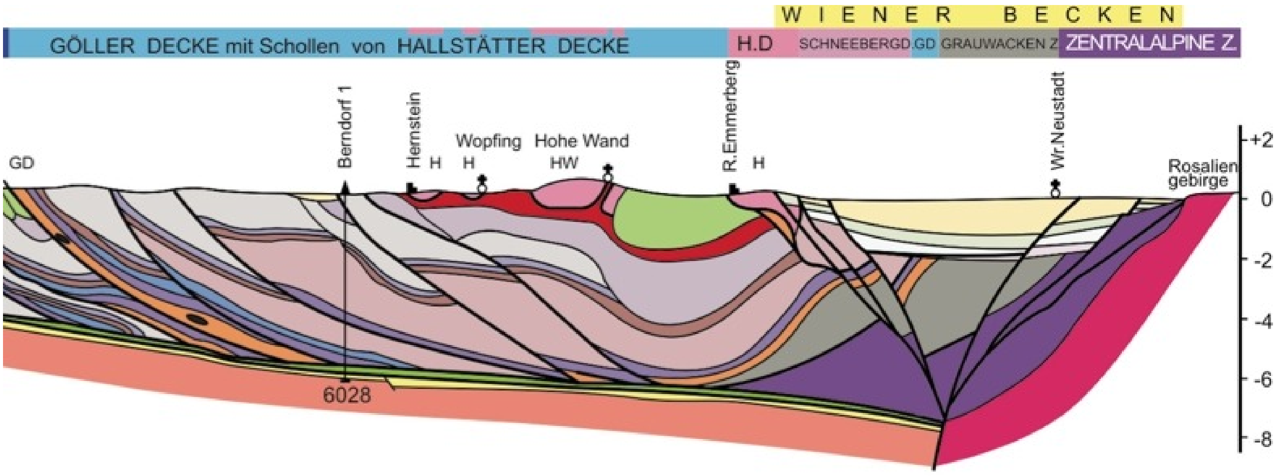

Figure 3: Section taken through the Vienna Basin showing how subsurface units eventually reach the surface as outcrops in the west. The Hohe Lindkogel is located approximately 10km north of the Berndorf 1 borehole. Right is Northeast, left is Southwest, scalebar in kilometers [Wessely, 2006].

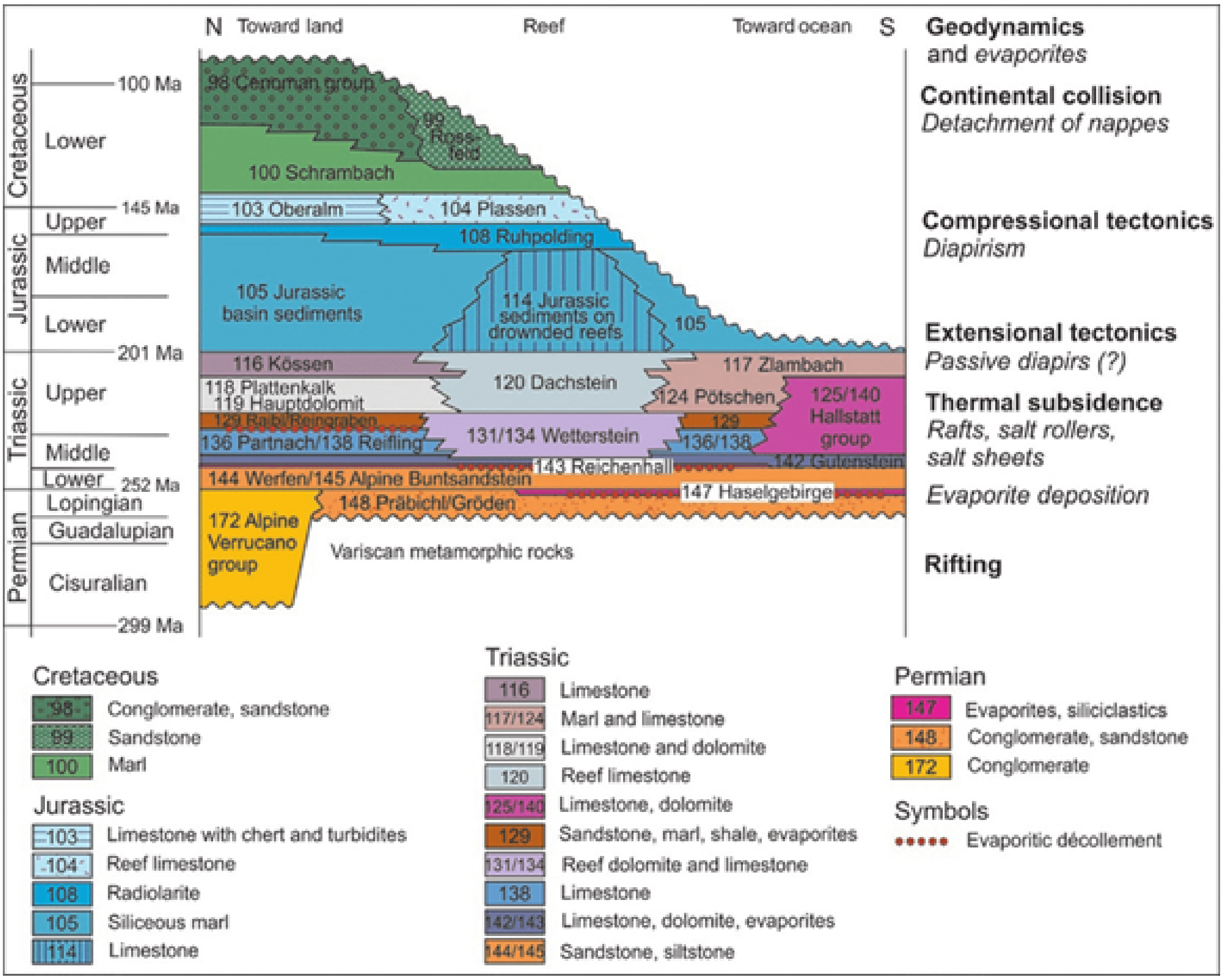

Figure 4: Schematic diagram of the alpine lithostratigraphic units, showing relative distance to the sea. Ramminger limestone/Dolomite is a sub-formation of the Reifling Fm. ([Leitner and Spötl, 2017]

4 Geology

4.1 Lithologies

The main Lithology being dealt with in this paper is the Wetterstein Dolomite present in the Göller and Schneeberg nappes.

It is however useful to define these lithologies, and the neighbouring lithologies as they are very similar in both appearance and depositional environment. These are very well described by A. Tollmann 1985 and G. Wessely 2006 and can be referenced to a more in-depth description including fossil content, as well as lithologies not mentioned here which are visible in Fig. 4. [Moser, 2023] also details the distribution of these lithologies around the Hohe Lindkogel and surrounding areas (Fig. 1). The following descriptions are sorted by age from youngest to oldest.

4.1.1 Dachstein Formation (Norian)

Consisting of limestone, this formation was deposited directly on top of the Wetterstein formation in the late Triassic during the Rhätian and Norian ages. These limestones are chemically unaltered and are abundant in fossils. Deposition of these limestones also occurred in the Meliata Ocean over a wide area of flat ocean and are up to 1500m thick in parts, constituting the higher parts of the calcareous Alps

[Tollmann, 1985].

4.1.2 Hauptdolomit Formation (Norian)

Another important dolomite formation which was deposited more inland from the Wetterstein formation in the late Triassic, likewise on the large carbonate platform. This Dolomite is much darker in colour due to the increased organic content present [Wessely, 1993].

In comparison to the Wetterstein dolomite, the Main Dolomite has undergone the dolomitization process more uniformly due to Mg enrichment by ingress of minerals by fluvial processes where the water then periodically evaporated and reflooded leaving behind the Mg ions [Fruth and Scherreiks, 1982].

4.1.3 Wetterstein Formation (Ladinium)

This unit is the primary research formation. These deposits represent coral reefs and lagoonal areas of the tropical shallow marine of the Tethys during the middle Triassic [Stampfli and Borel, 2002]. These waters developed a large carbonate platform from which the thick carbonate deposits of the alps are derived [Tollmann, 1985]. The distribution of lagoonal, reef, and fore-reef facies can be seen in Fig. 6.

Wetterstein Limestone (Lagoon): These limestones were deposited in the low energy, shallow back-reef area sheltered from the ocean. These limestones contain numerous fossils of sponges, corals, brachiopods, bivalves, and gastropods, and have a laminated structure typical of lagoonal deposition.

Wetterstein Limestone (Reef): A more front-reef representation, these limestones lack the lamination present in the lagoonal facies as these limestones consist of coral growths primarily.

Wetterstein Dolomite: One of the primary reservoir targets that we shall be analysing in this study. Also known as Ramsau Dolomite though the distinction is fuzzy [Tollmann, 1985]. This dolomite originates as lagoonal limestone depositions and subjected to dolomitization. Through this process recrystallization of the rock has largely destroyed any fossil content, and results in a harder, blocky rock that is well fractured. Some lamination has been preserved and other features such as partially cemented fractures and pores are present (Fig. 2). It is this fracturing and porosity that is essential for its importance in deep geothermal.

Compared to the Hauptdolomit Fm., the Wetterstein variant is much brighter as its organic content is much lower; in the Main Dolomite this organic content creates a dark grey appearance, allowing it to be easily distinguished [Tollmann, 1985].

The dolomitization process here happened as a result of algal species that incorporate much magnesium into their structure, causing a sporadic enrichment of Mg in the area, and driving dolomitization [Wessely, 2006]. This dolomite is considered to be early Diagenetic, with the the lagoonal areas most strongly affected by dolomitization, and the reef less so [Henrich and Zankl, 1986].

4.1.4 Reiflinger Formation (Anisian)

Another limestone formation showing deep sea/hemi-pelagic facies with a low sedimentation rate. These depositions occurred in the Anisian and Ladinium ages. Partial dolomitization of this

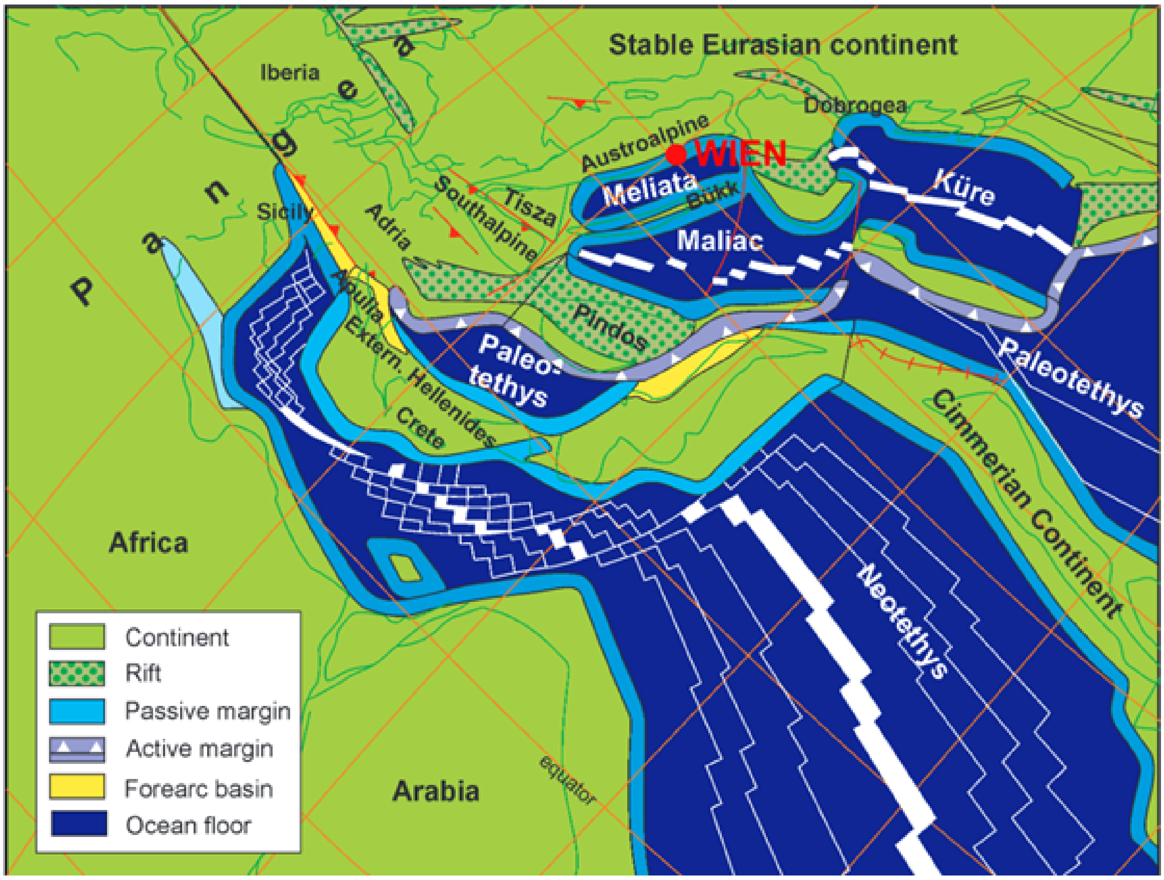

Figure 5: Paleogegraphic map of the location of Vienna during the Ladinium. (Franz Neubauer, 2019)

formation has occurred [Tollmann, 1985]. This unit is also of importance for geothermal exploration as it represents the lateral deepwater equivalent to the Wetterstein platform.

Raminger Kalk: A sub-formation of the Reiflinger Formation, which can also be found in dolomite form. This sub-formation is strongly present on the Hohe Lindkogel as dolomite (Fig. 1). It is present as the transition from Reiflinger Formation to Wetterstein Formation and represents the fore-reef area.

4.1.5 Gutenstein Formation (Anisian)

Laying on top of the Werfen Formation (Fig. 4), The Gutenstein Formation was deposited in the Anisian age of the lower Triassic. These limestones are dark in colour due to their high bitumen content from anoxic environments and poor water circulation [Faupl, 2000] and are intercrossed with calcite veins. This is a very thinly bedded unit with thicknesses from 50m to 250m, whose depositional facies is that of a shallow basin [Wessely, 2006]. This unit also features partial dolomitization of the limestones [Tollmann, 1985].

4.1.6 Werfener Formation (Skythian)

The Werfen Formation marks the beginning of the Triassic, and consist at their lowest level of reddish sandstones deposited in a tidally influenced area as a result of transgressive processes as the sea opened up at the end of the Permian. At higher levels of the formation the sandy deposits give way to more calcareous units and eventually to Werfen Limestone. [Wessely, 2006].

In total the Werfen Formation is around 500m thick, the lower sandy units consist of quartzite, and

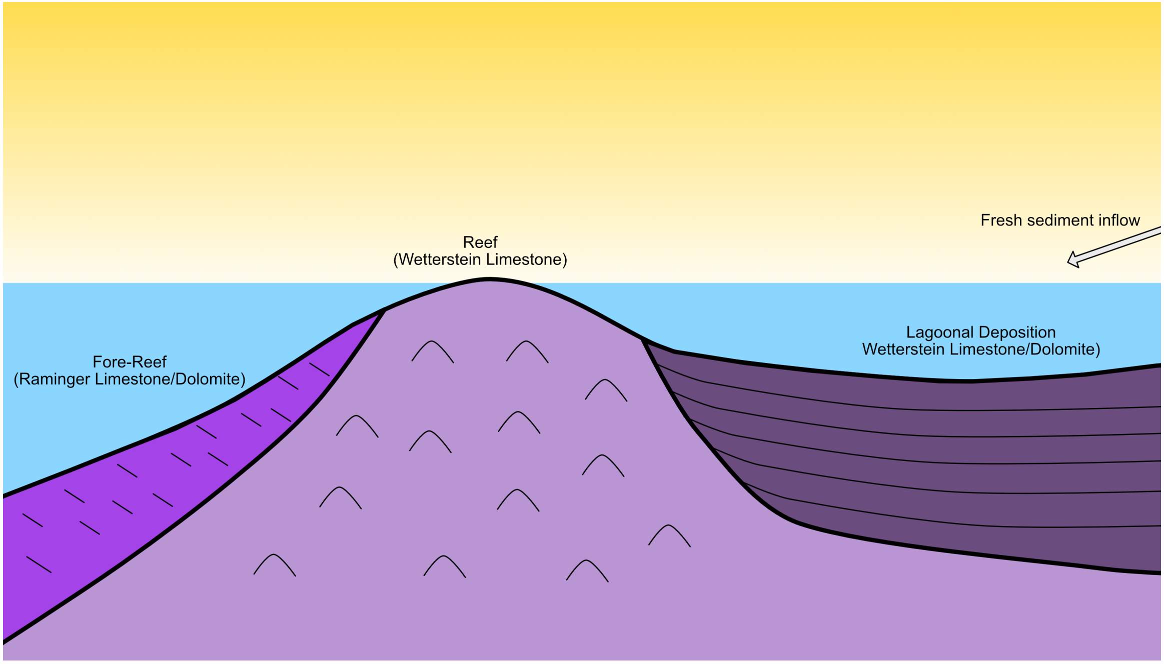

Figure 6: Schematic showing the general layout of the coral reef

are of a light-green to white colour. The upper units of the so-called Werfener Schiefer above, consist of clay sediments with heavily weathered micas. The last part of the unit is the Werfen Limestone on top, and is rich in various faunal species [Tollmann, 1985].

4.1.7 Haselgebirge Formation (Skythian)

These deposits represent evaporitic strata such as gypsum and halite along with clay minerals and sandstones. These are from the Permian-Triassic border, and deposited in a shallow sea within a Graben system in the Tethys. Regular seaswater incursions into the area created hypersaline waters which led to the evaporitic conditions [Mandl, Gerhard W., 1999]

4.2 Geologic Development

The area that we shall be operating in is around Wiener Neustadt. A part of the Northern Calcareous Alps (NCA) is located to the west and the Pannonian Basin located to the east.

The Pannonian Basin represents the old seabed of the Pannonian Sea that has then become filled in with Neogene sediments. This inland sea reached its largest extent during the Pliocene, and was gradually infilled by prograding deltas transporting sediments from the surrounding mountains [Kázmér, 1990].

The lithologies of the Northern Calcareous Alps are primarily the result of deposition in environments influenced by the Neotethys Ocean, which evolved through several stages during the Triassic to Jurassic periods. The Meliata Ocean, a smaller and more distal oceanic basin related to the Neotethys, was present during the same time frame (approximately 230 Ma to 180 Ma) but is more closely linked to the tectonic evolution southeast of the NCA. This period also saw the emergence of the Vardar Ocean, marking a later stage in the evolution of the Tethyan oceanic system [Stampfli and Borel, 2004].

The coastal areas of the Neotethys were part of a wide shelf area that hosted widespread carbonate platforms [Faupl, 2000].

The present geology and morphology of the area surrounding Wiener Neustadt is strongly influenced

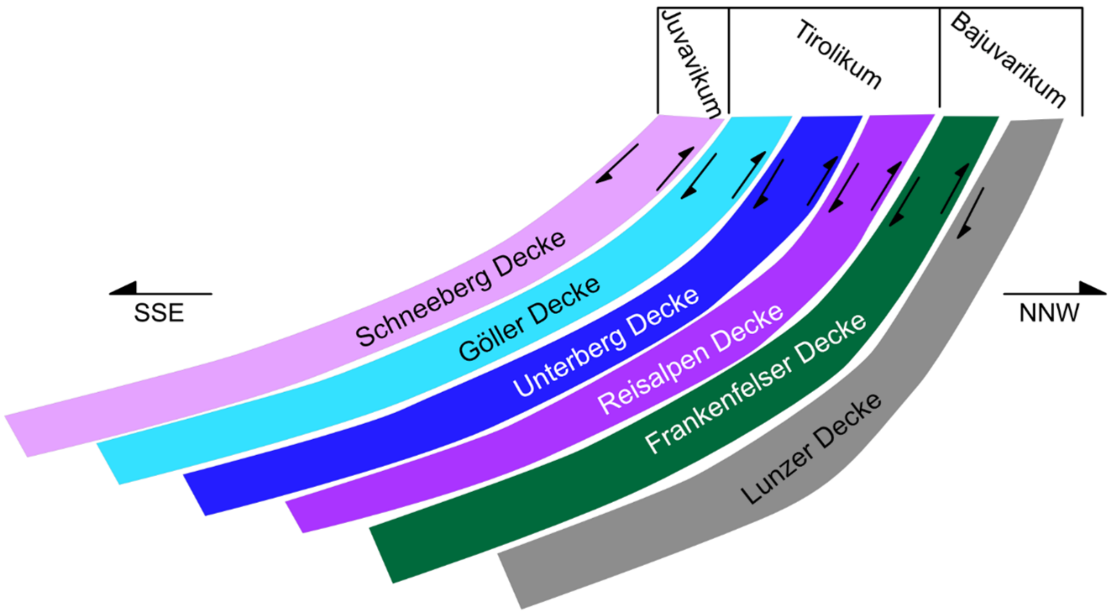

Figure 7: Schematic depiction of the Nappe system within the eastern NCA

by two main processes.

The first is the Alpine Orogeny; the collision of the Adriatic plate with that of Europe to produce the Alps. This period of mountain development had two stages to its development; the Eoalpine phase, and the Alpine phase. The Eoalpine phase was a precursor event (late Cretaceous) where the Adriatic plate briefly collided with the European plate before moving away again, and then colliding again for the main orogenic event in the Paleogene [Doglioni and Ferrara Bosellini, 1987].

The other Process is that of Glaciation. These cyclical processes strongly modify the morphology of the landscape by carving out huge quantities of rock and depositing them at their extents.

4.3 Tectonics

The tectonics of the Alps are extremely complicated and, in some parts, controversial due to the difficulty interpreting these tectonics.

The collision of the Adriatic plate with the European plate some 50 million years ago, caused the Alpine orogeny. This process resulted in heavy folding and thrusting of the sedimentary rocks resulting in various features such as the Tauern window, and the lateral strike-slip fault systems that developed, and resulted in the creation of the Carpathian Mountains by pushing out rock laterally to the east as the area was compressed.

In the eastern part of the NCA, the system can be described as being subdivided into a series of thrust units, called nappes. These units were thrust over one another during the Alpine orogeny. The individual nappes in the eastern portion are the Schneeberg, Göller, Unterberg, Reisalpen, Frankenfelser, and Lunzer Nappes (Fig. 7).

4.4 Hydrological Considerations

Around the Sollenauer fault area are a number of anomalous temperature readings from the boreholes in that area. This is most visible in the Sollenauer 001 borehole temperature measurement, where temperatures deviate significantly from the expected geothermal gradient. Such anomalies can be indicative of fluid movement along fault planes, suggesting that the fault may be acting as a conduit for either upward or lateral migration of warm fluids.

Faults, such as the Sollenauer, often have dual roles in groundwater systems: they may serve as conduits for fluid flow due to increased fracture permeability, or as barriers where sealing by fault gouge impedes flow. In the case of the Sollenauer fault, the observed anomalies suggest that the fault plane might be hydraulically active, allowing warm fluids from deeper strata to migrate toward the surface. This is supported by the sharp thermal gradient shifts, which are commonly associated with the presence of highly permeable fault zones [Curewitz and Karson, 1997].

The localized increase in temperature around the Sollenauer fault is likely caused by enhanced vertical permeability along the fault, allowing fluids heated at depth to rise more easily compared to surrounding areas. This phenomenon has been noted in several geothermal systems worldwide, where faults provide preferential pathways for fluid circulation [Sibson, 1996].

5 Methods

5.1 Sample Collection

Sample collection consists of identifying suitable outcrops on the Lindkogel and Schneeberg, marking their positions via GPS, and finally taking large samples approximately 10 cubic centimeters that can be utilized for plug permeameter tests and also for thermal conductivity studies that are not a part of this thesis.

Figure 8: Example of FDC1

Figure 9: Example of FDC2

Figure 10: Example of FDC3

Collected samples are marked appropriately with a short code, and the details of this sample are recorded in more detail in a field book.

Identification of samples is also necessary due to the partial dolomitization of the Wetterstein limestones in order to ensure that dolomite is indeed being collected. Hydrochloric acid is therefore used on the samples as limestones will fizz quite energetically, but dolomite will barely react at all.

The location being analysed contains Raminger Dolomite series which appears as thickly bedded carbonates consisting of clastic material deposited in front of the Wetterstein platform, as no suitable Wetterstein outcrop was available in the area.

The start and end location of each outcrop is measured by GPS coordinate using Bundesmeldenetz (EPSG 31259). The thickness and dip/dip direction of each bedded unit are then measured. This is done for the entire length of the road chosen (Fig. 1).

These measurements are imported into a GIS program with a high resolution DTM which enables the precise reading of height for each GPS point, which in turn allows the reconstruction of the entire profile allowing for gaps in the record and topology changes as outcrops only appear sporadically, and the road undulates in its altitude.

While measuring dip and dip direction, the Fracture Density Class (FDC) is also recorded. The following classification is adapted directly from [Theyer, 2022], based on [Decker, 2007] standards. It categorizes rock volumes according to the number and spacing of fracture sets:

- **FDC 1:** (Unfractured) Rock domains showing up to three fracture families with distinct orientations. Average fracture spacing exceeds 10 cm (Fig. 8). P32 ranges from 0 to 20 m^2/m^3.
- **FDC 2:** (Widely Fractured) Rock domains containing at least three differently oriented fracture families, with fracture spacing between 5 and 10 cm (Fig. 9). P32 values lie between 20 and 60 m^2/m^3.
- **FDC 3:** (Closely Fractured) Rock domains cut by more than three fracture families, showing spacings of 1–5 cm (Fig. 10). P32 varies from 60 to 200 m^2/m^3.
- **FDC 4:** (Very Closely Fractured) Rock domains affected by many fracture families, with fracture spacing $\leq$ 1 cm (no outcrop example available). P32 exceeds 300 m^2/m^3.

Note: This list is reproduced/adapted verbatim from Theyer (2022) to maintain technical accuracy.

The fracture density is one of the main factors affecting permeability, providing a good at-a-glance indication of the relative permeability; the higher the density, the more permeable the rock. These values shall then be correlated against mini-slug tests.

Further Considerations: The area in which the analyses were conducted was part of private land ownership belonging to the Austrian Federal Forestry Commission, and also part of a nature reserve. This meant that specific authorizations had to be obtained first from the state of Lower Austria to be able to operate within the nature reserve, and also from the Forestry Commission to use their roads.

5.2 Profile Reconstruction

Where possible, a series of continuous outcrops spanning a large thickness of the formation was located. On the Lindkogel the dolomite formations there are approximately 200m thick in total and bedded which allows for the recording of strike and dip. The bed thicknesses are all recorded along with the strike and dip using a geological compass and also any features visible in the beds. Gaps between outcrops are compensated for by calculating the thickness missing from geodesy scans (laser) in order to get the most accurate measurements possible. These recordings are used to create a log of the outcrop, and also the profile based on the dip and strike data.

Figure 11: Mini-slug tests mounted

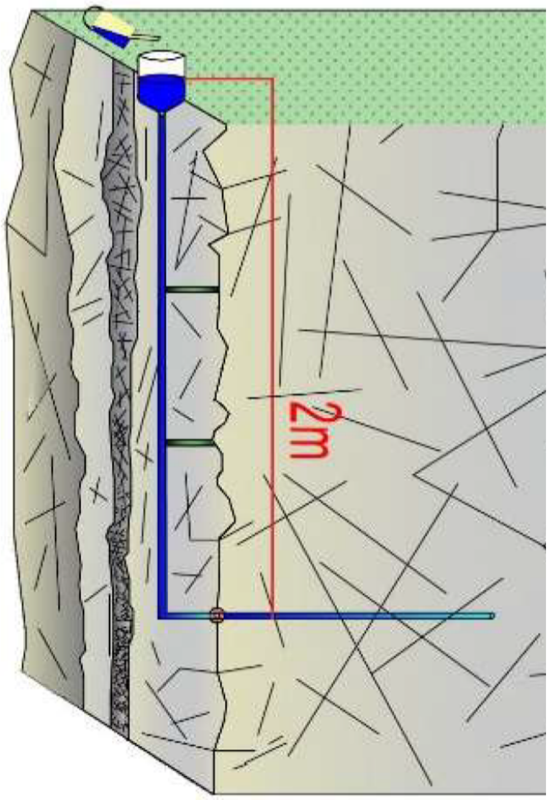

Figure 12: Mini-slug test schematic [Pirmoradi, 2022]

5.3 Porosity measurements by immersion technique

Porosity can be calculated by using the immersion method. This method is covered by ÖNORM standards EN 1936 (2006). Samples to be measures must first be completely dry and are therefore placed in an oven at about 100°C for a minimum of 24 hours. After this period the sample is weighed and then placed again in the oven for a further 24 hours. The sample is weighed again and checked against the original measurement for any deviation. A deviation of more than 0.1 percent is unacceptable, and the drying process is repeated until the deviation is within the specified limits.

The completely dried and weighed sample that is within the tolerance is then submerged in a demineralized water bucket. The sample is allowed to soak for 24 hours so that the sample becomes saturated. The sample is removed and any surface water on the sample is dried off. The sample is then weighed, and the process repeated for another 24 hours until the weight deviation is again less than 0.1 percent between measurements.

Finally, the sample is measured whilst submerged for 24 hours, and measurements are repeated until the same tolerance is achieved. The following values are obtained:

- Md = Mass of dry sample
- Mh = Mass of submerged sample
- Ms = Mass of saturated sample

With these values we can utilize the following formula to obtain the Grain Density of the sample:

$$\rho = \frac{M_d * \rho_{H_2O}}{M_s - M_h} \tag{1}$$

where:

- ρ = grain density
- ρH_2O = density of water

The open porosity can also be determined in a similar way using the measured values. The open porosity is the porosity that is connected together throughout the sample allowing fluids to flow through. Closed porosity are isolated pores inaccessible to fluids.

Open porosity is calculated with the following equation:

$$p_o = \left(\frac{M_s - M_d}{M_s - M_h}\right) \cdot 100 \tag{2}$$

5.4 Porosity and Permeability Measurements with the Coreval 700

5.4.1 Sample Preparation

The Porosity/Permeameter, sometimes referred to as PoroPerm, is a device used to quickly determine the porosity and permeability characteristics of a small rock sample known as a plug. Plugs are drilled from a larger rock sample, which must be sufficiently large to produce a minimum of 12.7 mm (1/2”) and a maximum of 76.2 mm (3”) in length, with a diameter of 38.1 mm (1.5”). The plug ends must be flat, smooth, and perpendicular to the plug cylinder axis.

Samples must also be completely dry to avoid erroneous readings from residual fluids. Drying in an oven for 24 hours is recommended to remove all moisture.

5.4.2 Coreval 700 Function

The following section provides a description of the technical operation and measurement principles of the Coreval 700 gas-permeameter and porosimeter, based on the manufacturer’s operating manual [Vinci Technologies, 2013] and related sources [Theyer, 2022]. All equations and methodology are presented to explain the measurement procedure, not as original derivations.

The device available is the Coreval 700, which uses nitrogen (N_2) as the working gas for both porosity and permeability measurements [Vinci Technologies, 2013]. Porosity measurements are based on the *Boyle’s Law Single Cell Method* for direct void volume measurement, as recommended by the API. Permeability measurements follow *Darcy’s law* and the Pressure-Falloff (unsteady-state pressure drop) method.

5.4.3 Porosity Measurement

Gas is introduced into a sealed chamber containing the rock plug. Using the ideal gas law:

$$PV = nRT, \tag{3}$$

the total moles in the system can be expressed as

$$n_{\text{total}} = \frac{P_1(V_r + V_v)}{Z_{N_2}RT} + \frac{P_a(V_d + V_p)}{Z_{\text{air}}RT}, \tag{4}$$

where V_r is the reservoir volume, V_v the valve volume, V_d the dead volume, and V_p the pore volume of the sample. Z_{N_2} and Z_{air} are compressibility factors. Assuming $P_1 \gg P_a$ and $n_{N_2} \gg n_{\text{air}}$:

$$n_{\text{total}} \approx \frac{P_2(V_r + V_v + V_d + V_p)}{Z_{N_2}(2)RT}. \tag{5}$$

Solving for the pore volume:

$$V_p = \frac{V_r \frac{P_1 Z_{N_2}(2)}{P_2 Z_{N_2}(1)} - 1 - V_v}{1 - \frac{P_a Z_{N_2}(2)}{P_2 Z_{\text{air}}}} - V_d, \tag{6}$$

and the porosity is

$$\phi = 100 \cdot \frac{V_p}{BV}, \quad BV = \frac{\pi D^2}{4} \cdot L. \tag{7}$$

High confining pressures require correction using the grain volume:

$$GV = BV - \phi, \quad \phi_{\text{corrected}} = \frac{V_p}{GV + V_p}. \tag{8}$$

Table 1: Variables for Porosity Measurements (adapted from Vinci Technologies, 2013; Theyer, 2022)

Variable	Description
P_1	Initial pressure in reservoir [Psi]
P_a	Initial pressure in dead volume [Psi]
P_2	Final pressure [Psi]
V_r	Reservoir volume [cm^3]
V_v	Valve volume [cm^3]
V_d	Dead volume [cm^3]
V_p	Pore volume [cm^3]
BV	Bulk volume [cm^3]
D	Sample diameter [mm]
L	Sample length [mm]
GV	Grain volume [cm^3]
Z_{N_2}, Z_{air}	Compressibility factors

5.4.4 Permeability Measurement

The permeability measurement begins by pressurizing the gas reservoir on the inlet side, while the end of the sample is vented to atmospheric pressure. Once thermal equilibrium is reached, an outlet valve is opened, resulting in transient pressure behavior. Data collection begins when the gas pressure drops to 85% of its initial value. The change in pressure over time allows calculation of the permeability [Vinci Technologies, 2013].

Gas permeability is affected by the mean free path of the flowing gas, causing the *slip effect*. The Klinkenberg correction adjusts for this:

$$K_g(x,t) = K_1 \left(1 + \frac{b}{P_{x,t} + P_a}\right), \tag{9}$$

$$K_g = K_1 \left(1 + \frac{b_m \mu_c}{\mu_m} \sqrt{\frac{T_c M_m}{T_m M_c}} \cdot \frac{1}{2P_g P_a}\right), \tag{10}$$

where K_g is gas permeability, K_1 the Klinkenberg (liquid) permeability, b and b_m slip factors, $P_{x,t}$ pressure at position x and time t, P_a atmospheric pressure, μ viscosities, T temperatures, M molecular weights, and P_g geometrical mean pressure [Theyer, 2022].

Table 2: Variables for Permeability Measurements (adapted from Vinci Technologies, 2013; Theyer, 2022)

Variable	Description
K_g	Gas permeability [mD]
K_1	Klinkenberg (liquid) permeability [mD]
b, b_m	Slip factor [Psi]
$P_{x,t}$	Pressure at position x and time t [Psi]
P_a	Atmospheric pressure [Psi]
μ_c, μ_m	Theoretical and measured gas viscosity [cP]
T_c, T_m	Theoretical and measured temperature [°F]
M_c, M_m	Theoretical and measured molecular weight [g/mol]
P_g	Geometrical mean pressure [Psi]

Maximum measurable pressure is 10000 Psi, covering the range of most permeability and porosity changes in the study area. The Klinkenberg correction is particularly important at low pressures (400 Psi) to obtain permeability comparable to liquids.

5.5 Mini Slug Test

This slug test is a smaller application of the well-focused slug test that can be conducted on exposed rock surfaces, and with minimal equipment. This method was pioneered by [Pirmoradi, 2022], the details of its application are detailed below.

A protocol sheet is prepared that includes all the details of the test and includes the following information:

- Borehole Name
- Date
- Geologist Name
- Rock Formation
- Lithology
- Fracture Density Class
- Water Temperature
- Hydrological Conditions
- Pressure Head
- Borehole Diameter
- Borehole Length
- Pipe Overlap
- Exfiltration through Rock Surface
- Time Interval Measurements

A hole of known diameter is drilled into the rock to a sufficient depth of about 0.5 -1 meter. The hole is then cleaned out to remove any dust that may block fractures and pores within the hole as this would invalidate any results. The depth of the hole is also measured at this point and noted down.

A tube with sealant is then forced into the hole, and a hand pump is attached in order to check whether the hole is valid for the slug test; often it is the case that when drilling a fracture or open space is discovered deep in the rock which allows water to flow unhindered from the test and producing an invalid test. The depth of the pipe in the hole is also noted here and is subtracted from the depth of the hole during the calculation phase.

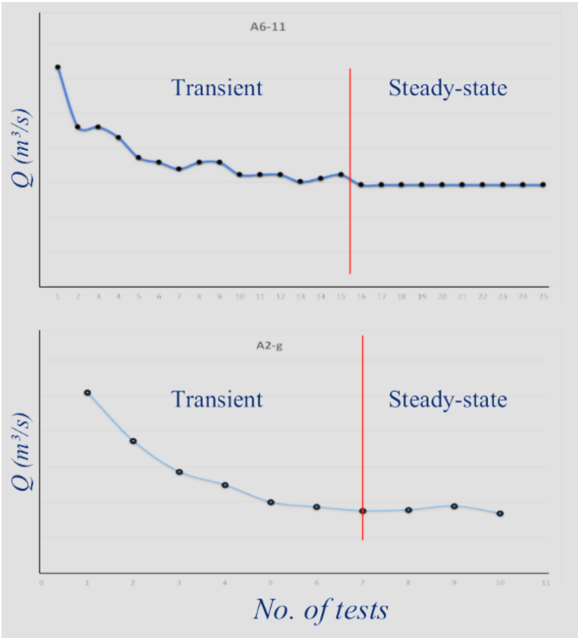

Figure 13: Time-series plot of flow rate from the mini-slug tests

Once the validity of the hole is established another tube fixed to a water container at one end is then attached to the tube in the rock, and the contained is fixed to the rock approximately 1.5 – 2 meters above the hole. This then provides the pressure head for the experiment. The height is accurately measured for the protocol. (Fig. 11)

The container is filled up with water and a line is marked on the container at the water line. The test now begins, and the start time is noted on the protocol (Fig. 12. Alternatively, a stopwatch can be affixed to the test too to track the time more easily. The container is repeatedly filled up to the line using water of known quantity carefully measured out in a bottle (in our case 250ml). once the 250ml has been emptied into the test container and the water is once again at the marked line, the time is noted, or the stopwatch stopped, and the elapsed time noted. The test is then repeated many times until the time interval reaches a steady state as the initial attempts will be faster as the rock is unsaturated. Sometimes however the permeability is so low that it is not possible to take more than one measurement, however this is acceptable in our case as the results need not be so accurate below a certain permeability.

Once the tests are complete and the data fully recorded, an average time of steady state measurement points can be taken from those results with sufficient recording points, and a calculation is made to determine the transmissivity.

The calculation used is a modification of the the Dupuit-Thiem well formula [Hölting and Coldewey, 2013] for calculating flow rate, reorganized to calculate for transmissivity and then using the relation between transmissivity (k_f) and permeability to gain the permeability (k) [Penz-Wolfmayr et al., 2022]:

$$k_f = \frac{Q/\Delta H}{2\pi L} \ln\left(\frac{L}{r_1}\right) \tag{11}$$

- k_f = Hydraulic Conductivity (m/s)
- Q = Flow Rate (m^3/s)
- ΔH = Pressure Head (m)
- L = Borehole Depth (m)
- r_1 = Borehole Diameter (m)

$$k = \frac{k_f \cdot \eta_f}{\rho_f \cdot g} \tag{12}$$

- k = Permeability (m^2)
- η_f = Dynamic viscosity of fluid (kg/ms)
- ρ_f = Fluid density (kg/m^3)
- g = Gravitational constant (m/s^2)

6 Results

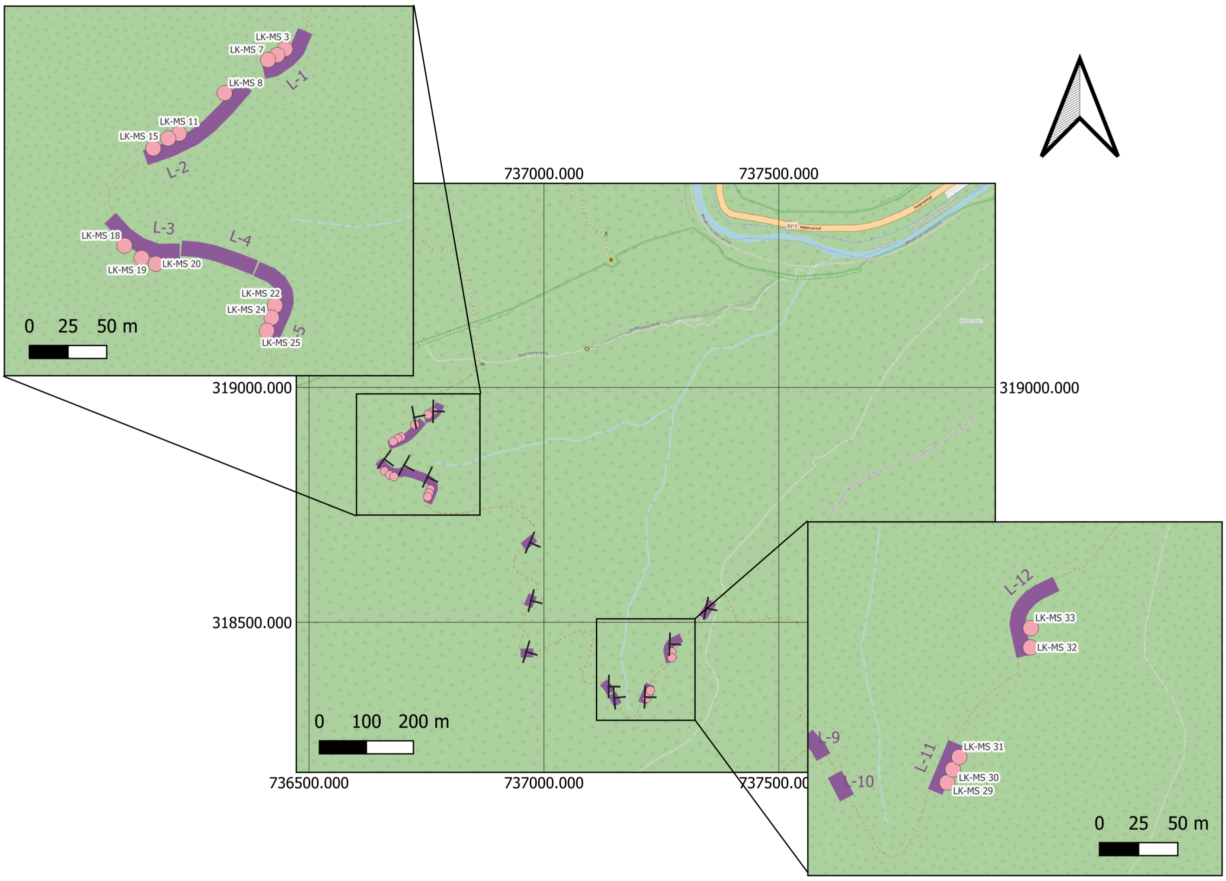

Figure 14: Overview map of the collected data points showing mini-slug tests, denoted by LK-MS prefix, and the outcrop lengths denoted by L prefix

The collected results without any interpretation are included in this section. Immediately below is a table (Table 3) will all results and the type of test, along with a map showing the locations of individual samples collected and the lengths of the outcrops (Fig. 14).

Sample	East	North	Immersion Porosity	Constant Head Slug Test	Gas Permeability	FDC
L1/5	736758	318945	X			3
L1/9	736754	318941	X			3
L1/10	736753	318942	X			3
L6/1	736972	318673	X			2
L6/10	736962	318664	X			2
L8/2	736724	318920	X			3
L9/1	737131	318364	X			3
L11	737212	318336	X			2

Sample	**East**	**North**	**Immersion Porosity**	**Constant Head Slug Test**	**Gas Permeability**	**FDC**
LK-MS 5	736758	318945	X	X	X	3
LK-MS 7	736753	318941	X	X	X	3
LK-MS 8	736724	318920	X	X	X	1
LK-MS 11	736695	318894	X	X	X	1
LK-MS 12	736688	318891	X	X	X	2
LK-MS 13	737345	318522	X		X	
LK-MS 15	736678	318884	X	X	X	3
LK-MS 18	736660	318821	X	X	X	2
LK-MS 19	736671	318813	X	X	X	2
LK-MS 20	736680	318810	X	X	X	2
LK-MS 22	736757	318783	X	X	X	2
LK-MS 24	736755	318775	X	X	X	2
LK-MS 25	736752	318766	X	X	X	2
LK-MS 29	737218	318338	X	X	X	3
LK-MS 30	737222	318346	X	X	X	3
LK-MS 31	737226	318354	X	X	X	3
LK-MS 32	737272	318424	X	X	X	2
LK-MS 33	737272	318436	X	X	X	2

Table 3: Consolidated table of all samples with all measurement types and FDC.

6.1 Orientation of Bedding

The outcrops of the Ramminger Dolomite show extremely well bedded profiles. The individual beddings were measured for thinkness and dip/sipdirection and later the total thickness of the entire visible formation was reconstructed to determine the minimum thickness of the dolomite formation. these outcrops are shown as the purple lines on figure 14, marked sequentially L-1 to L-13. Additionally, the height of each outcrop was acquired from a DEM.

Table 4 shows the average FDC and dip/dip direction for each outcrop, the full dataset can be seen in the appendix

Log	Total Thickness (cm)	Avg FDC	Dip/Direction	Height (m over Adria)
L1	1400	3	91/38	535,9
L2	3720	3	79/42	531,9
L3	760	3	126/47	520,8
L4	1860	3	119/51	514,9

Log	Total Thickness (cm)	Avg FDC	Dip/Direction	Height (m over Adria)
L5	1085	3	115/43	511,4
L6	210	2	113/48	505,2
L7	75	3	104/39	495,6
L8	289	3	107/44	496
L9	180	3	91/46	494,2
L10	235	3	85/44	494,2
L11	580	2	92/34	496,8
L12	900	3	92/62	503,5
L13	580	2	101/36	507,3

Table 4: Average values for each outcrop

6.2 Mini Slug Tests

17 constant head mini slug tests were conducted over a period of 2 weeks from the 01.10.2024 to the 04.10.2024 and from 16.10.2024 to 17.10.2024. The following graphs show the results of each slug test with the k value on the y axis, and the test number on the x axis. All original data can be found in the appendix.

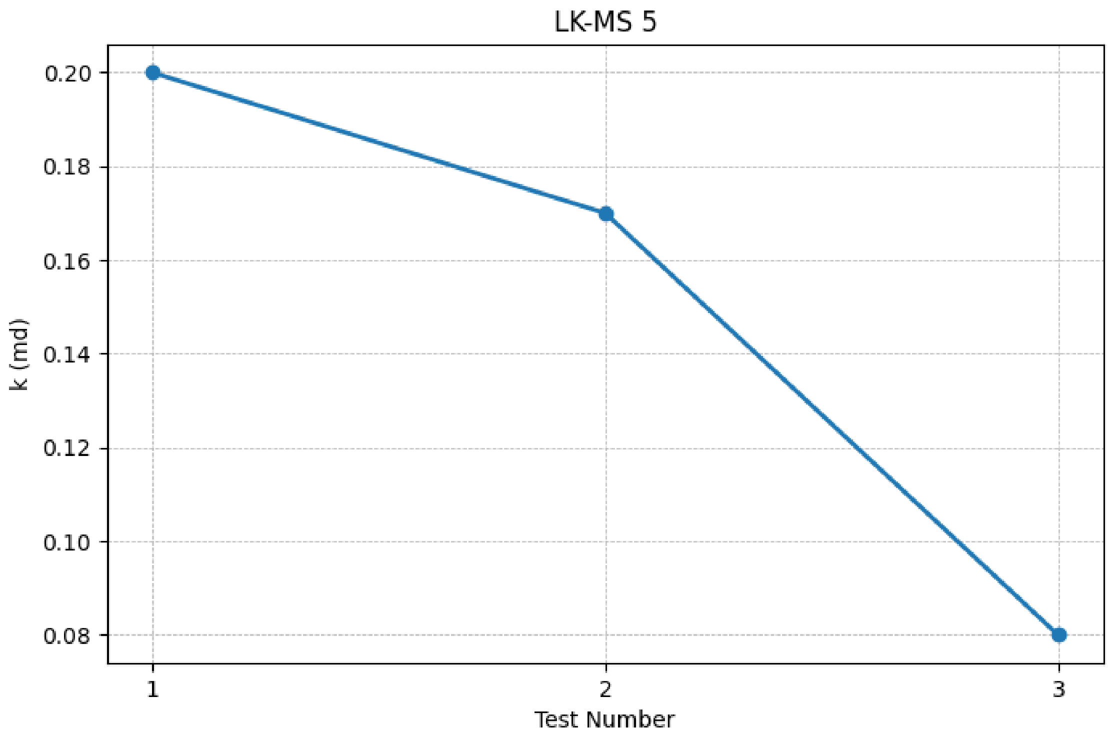

Figure 15: LK-MS5 permeability results

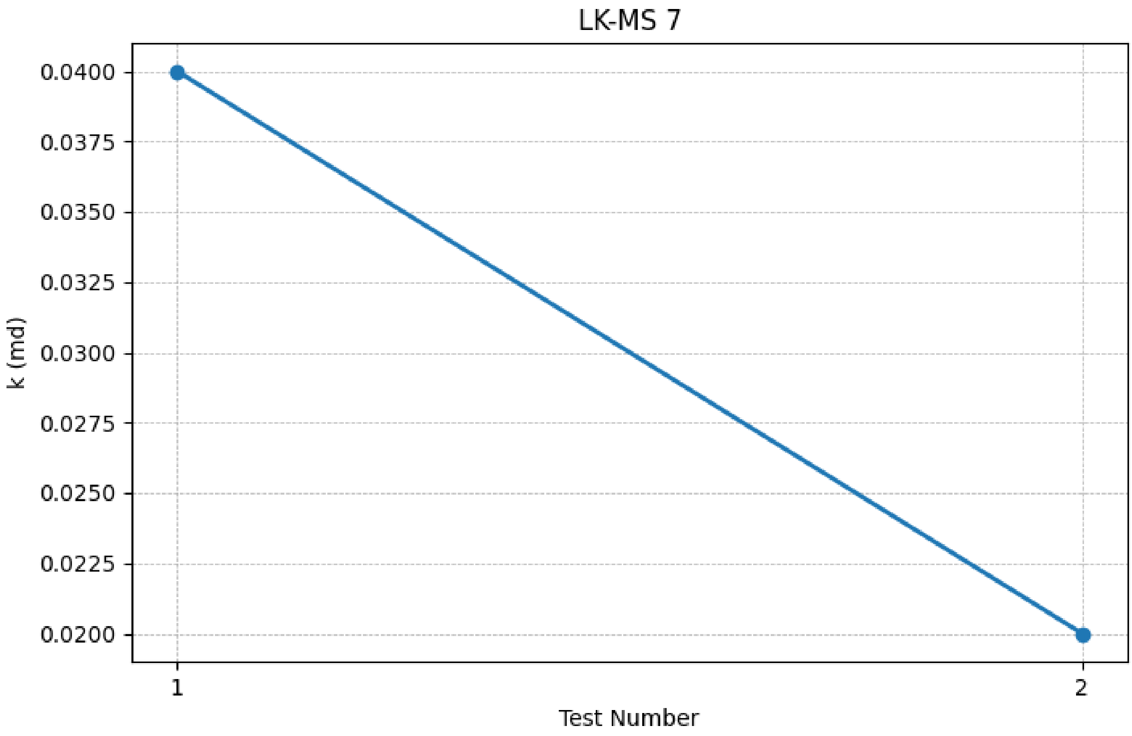

Figure 16: LK-MS 5 permeability results

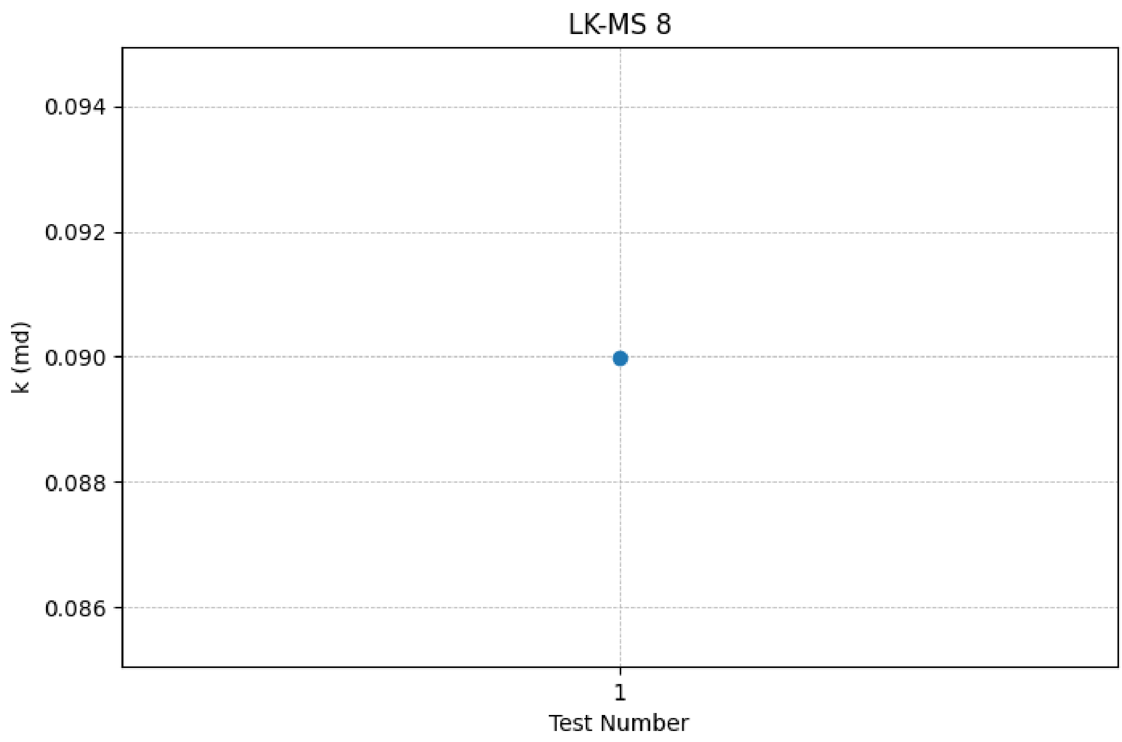

Figure 17: LK-MS 7 permeability results

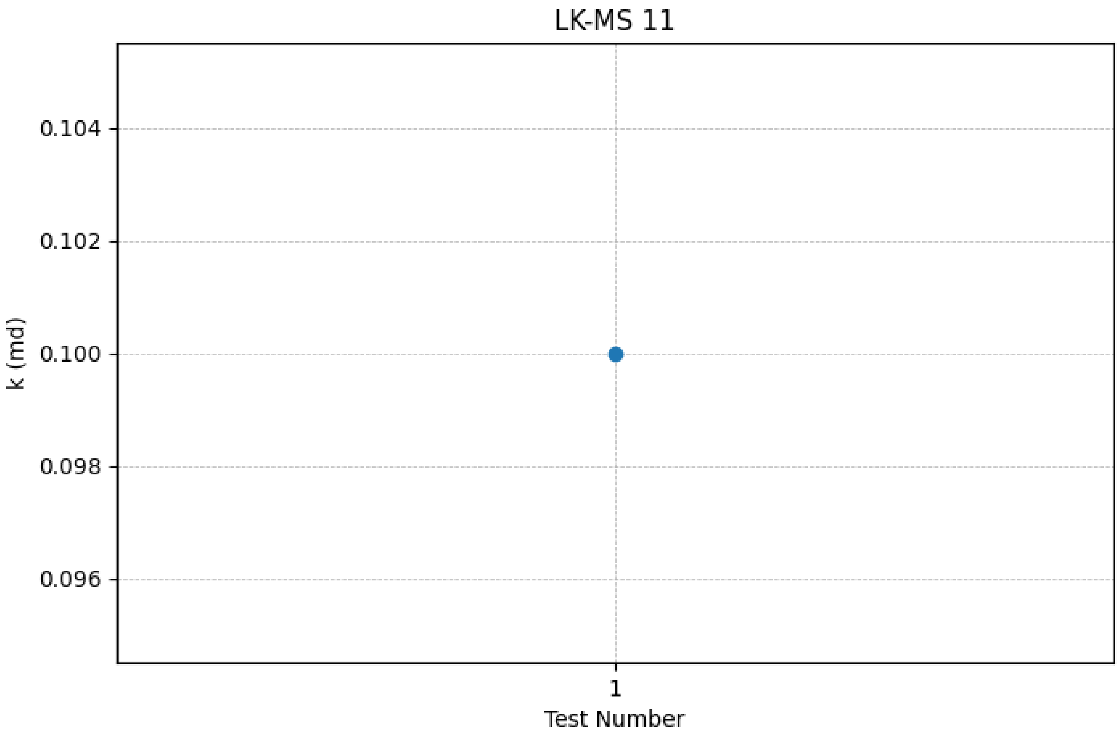

Figure 18: LK-MS 11 permeability results

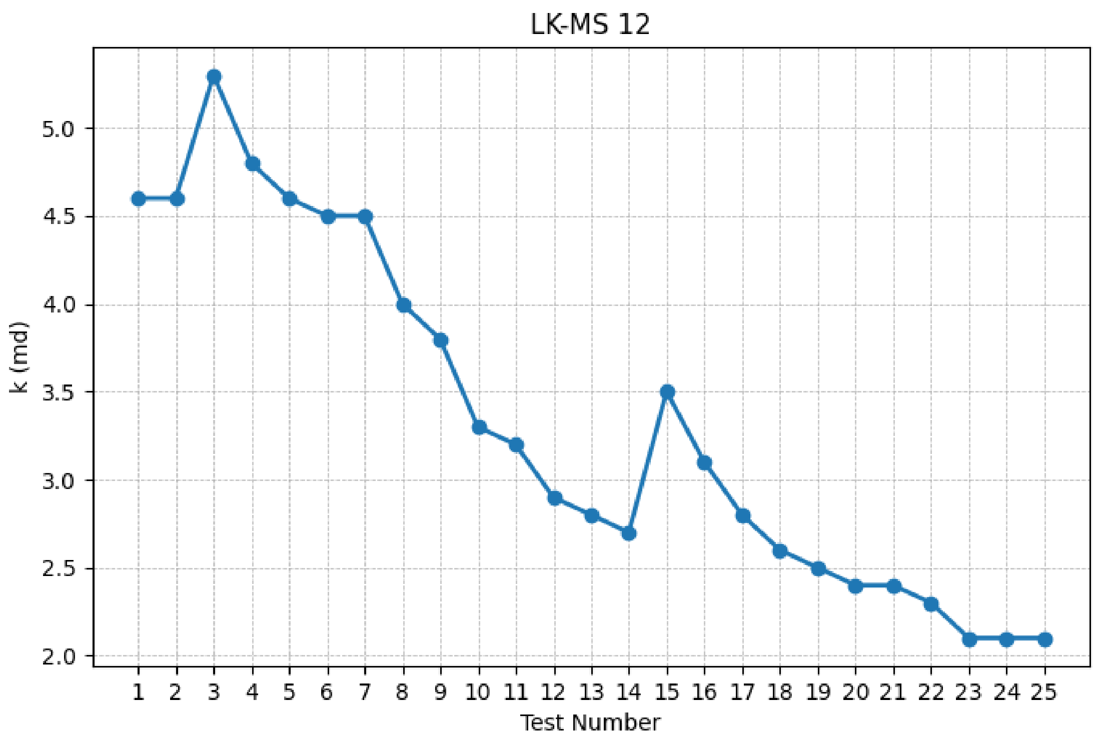

Figure 19: LK-MS 12 permeability results

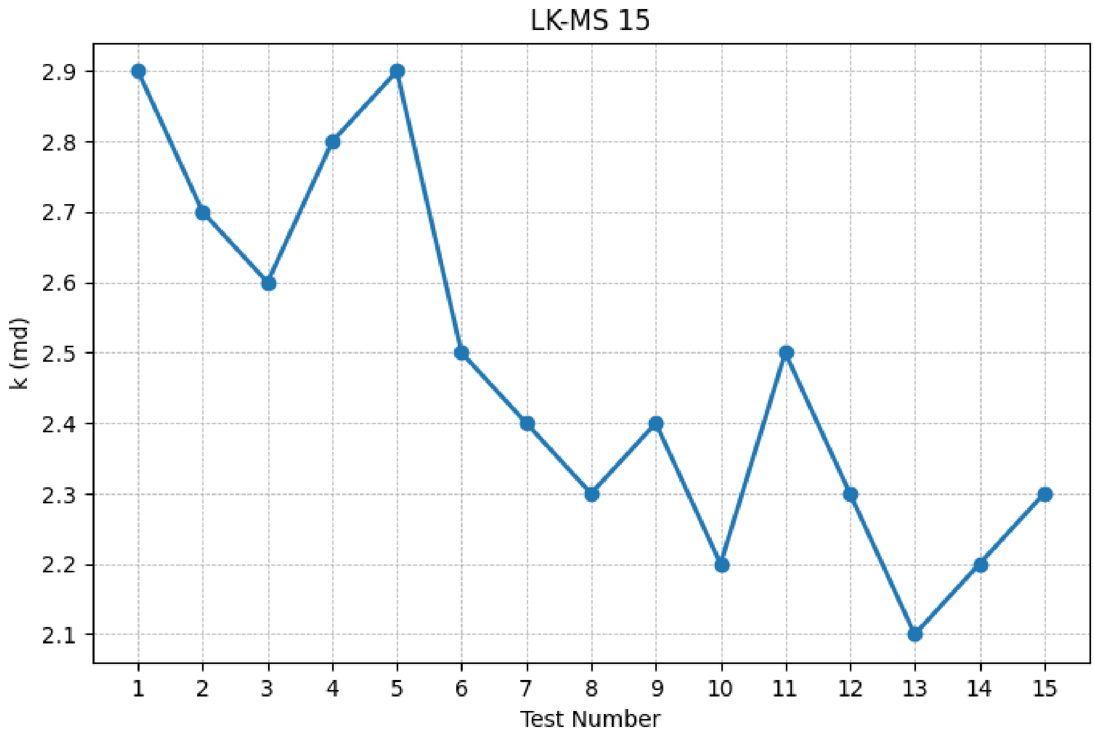

Figure 20: LK-MS 15 permeability results

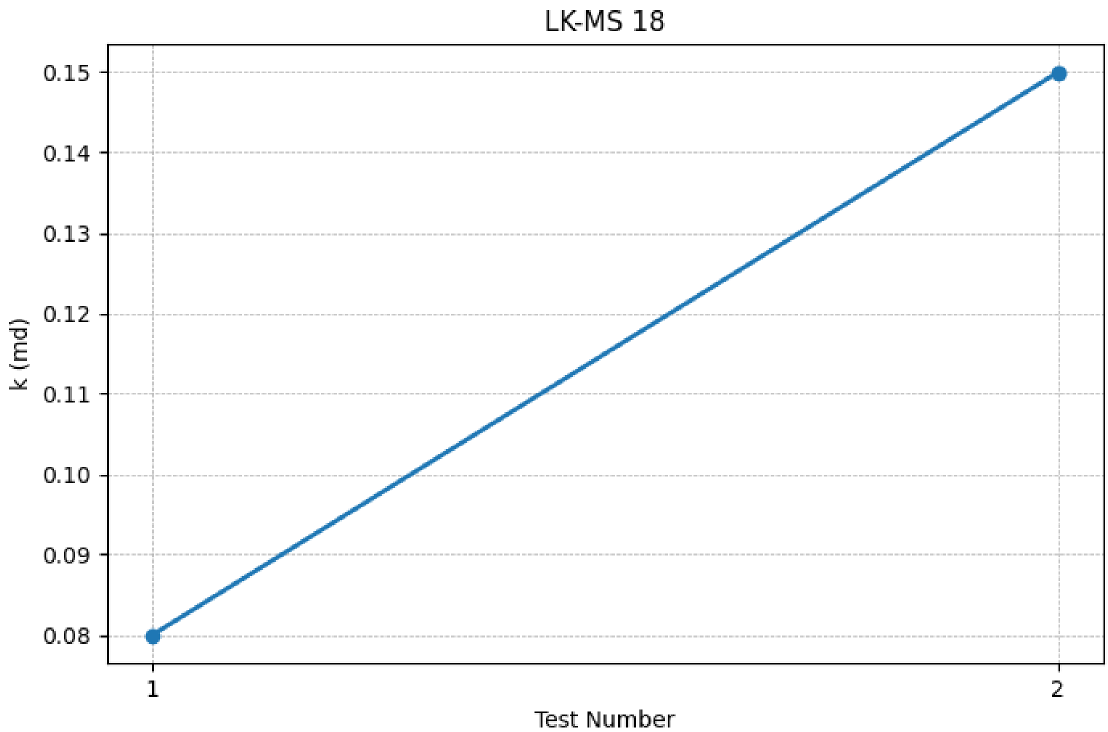

Figure 21: LK-MS 18 permeability results

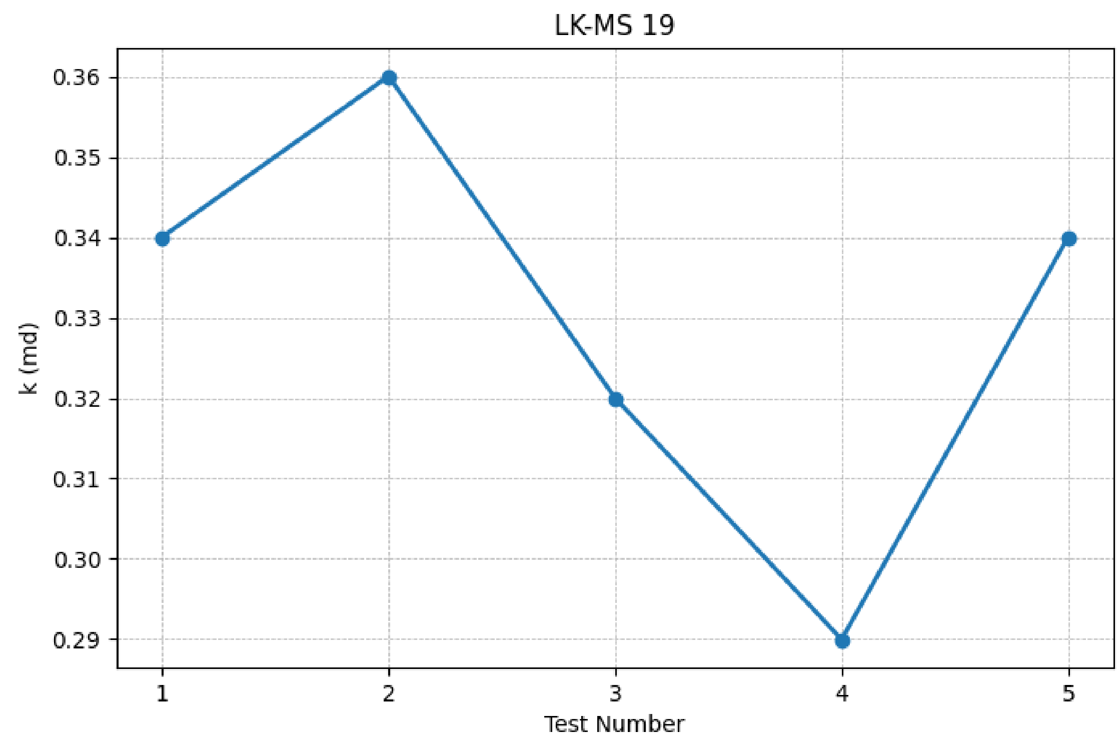

Figure 22: LK-MS 19 permeability results

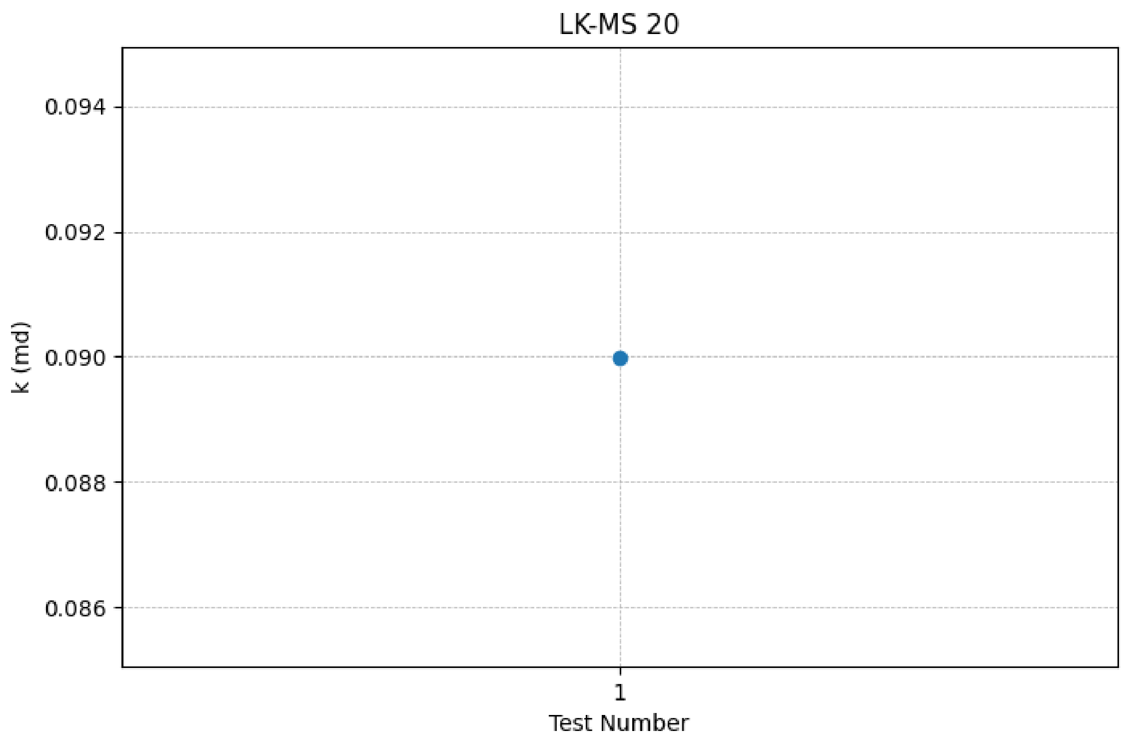

Figure 23: LK-MS 20 permeability results

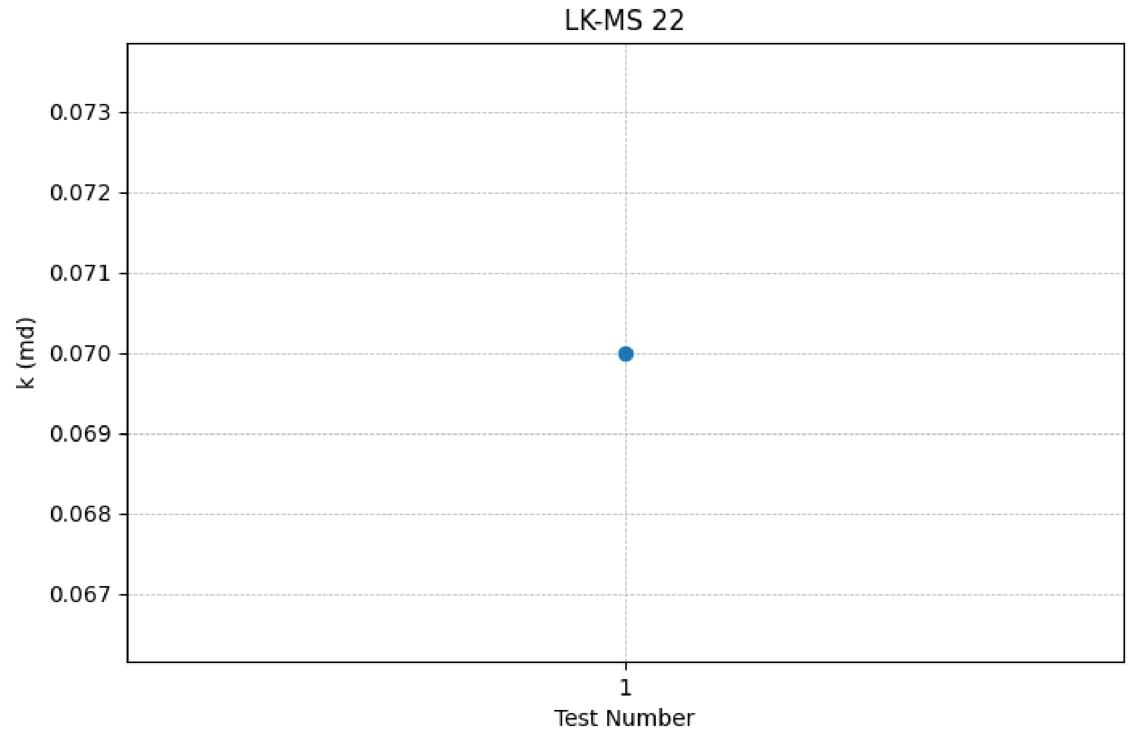

Figure 24: LK-MS 22 permeability results

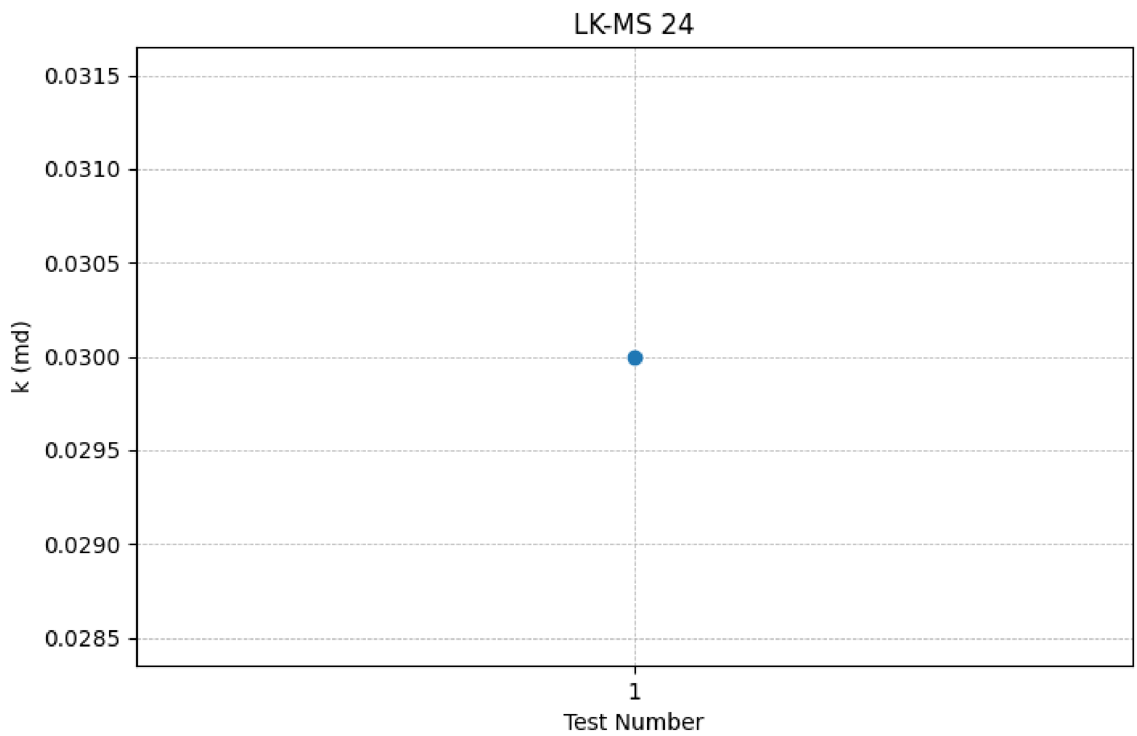

Figure 25: LK-MS 24 permeability results

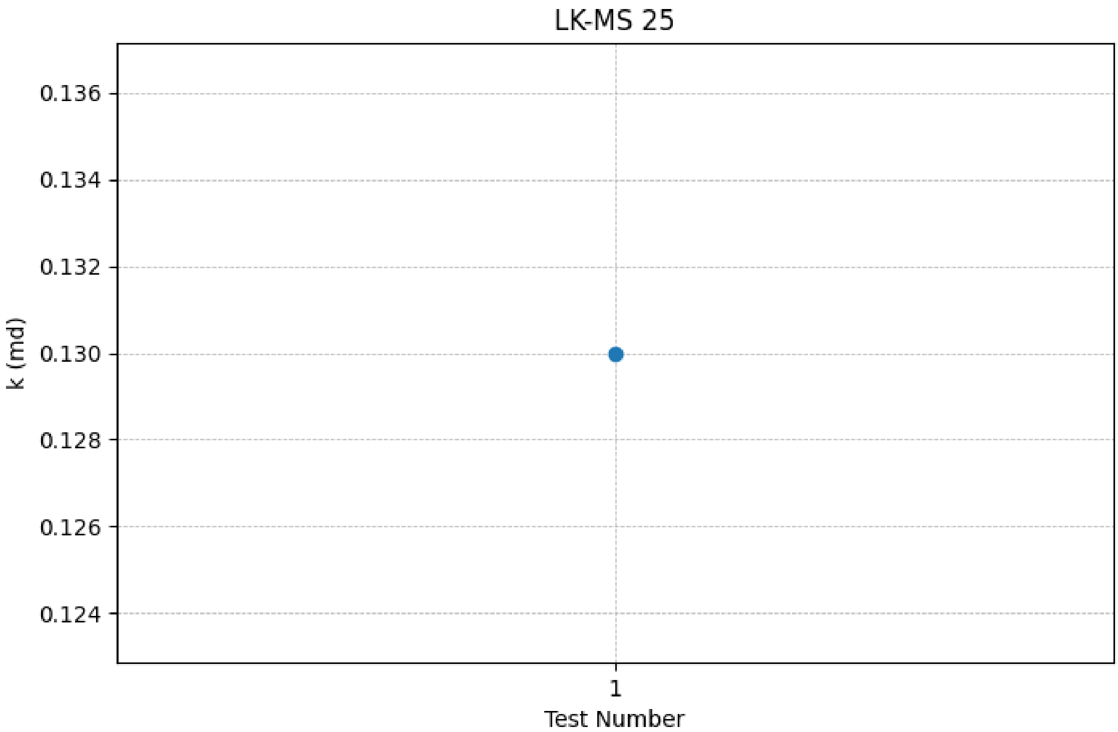

Figure 26: LK-MS 25 permeability results

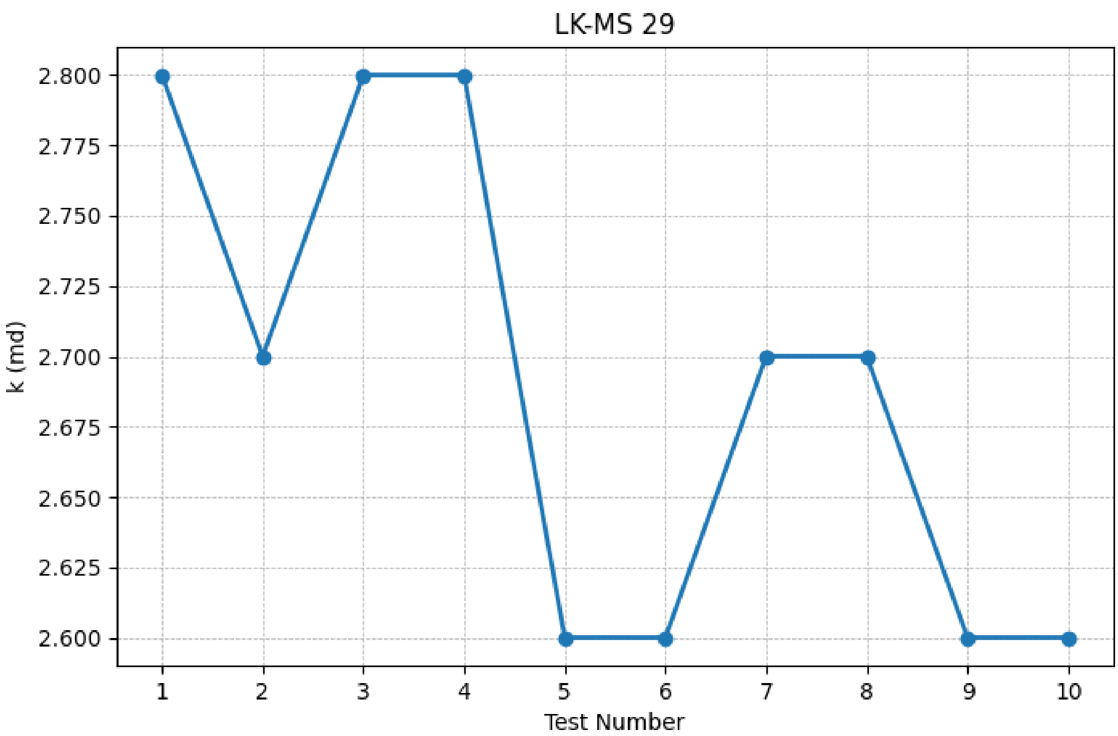

Figure 27: LK-MS 29 permeability results

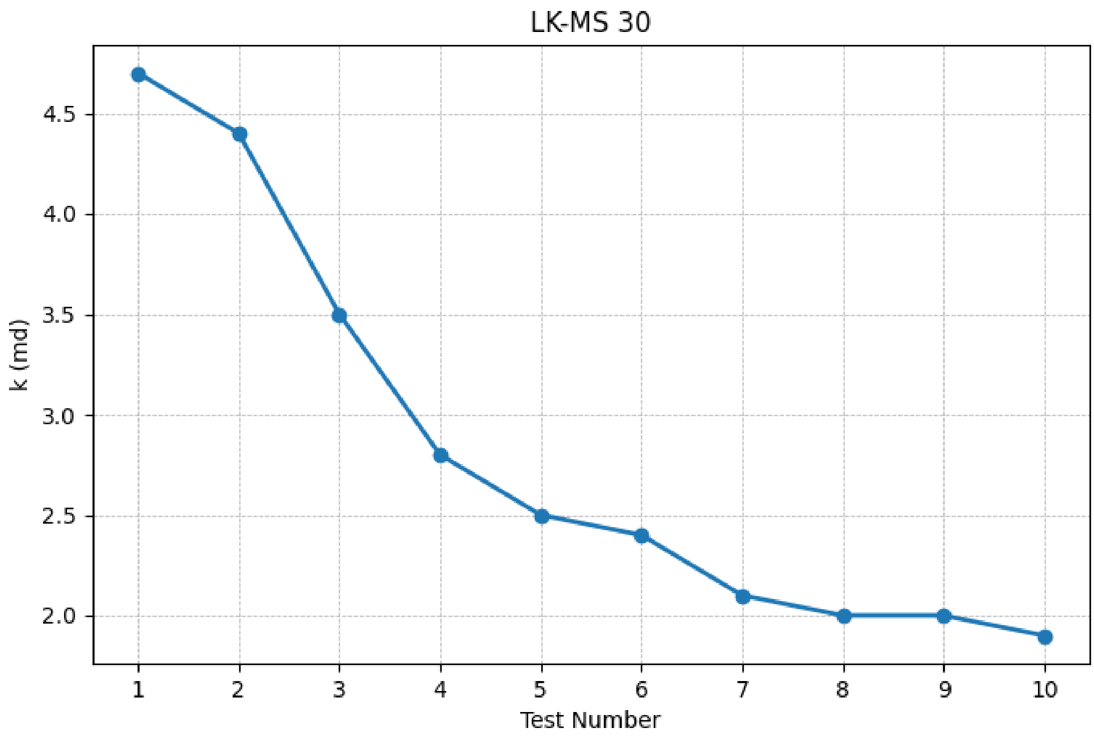

Figure 28: LK-MS 30 permeability results

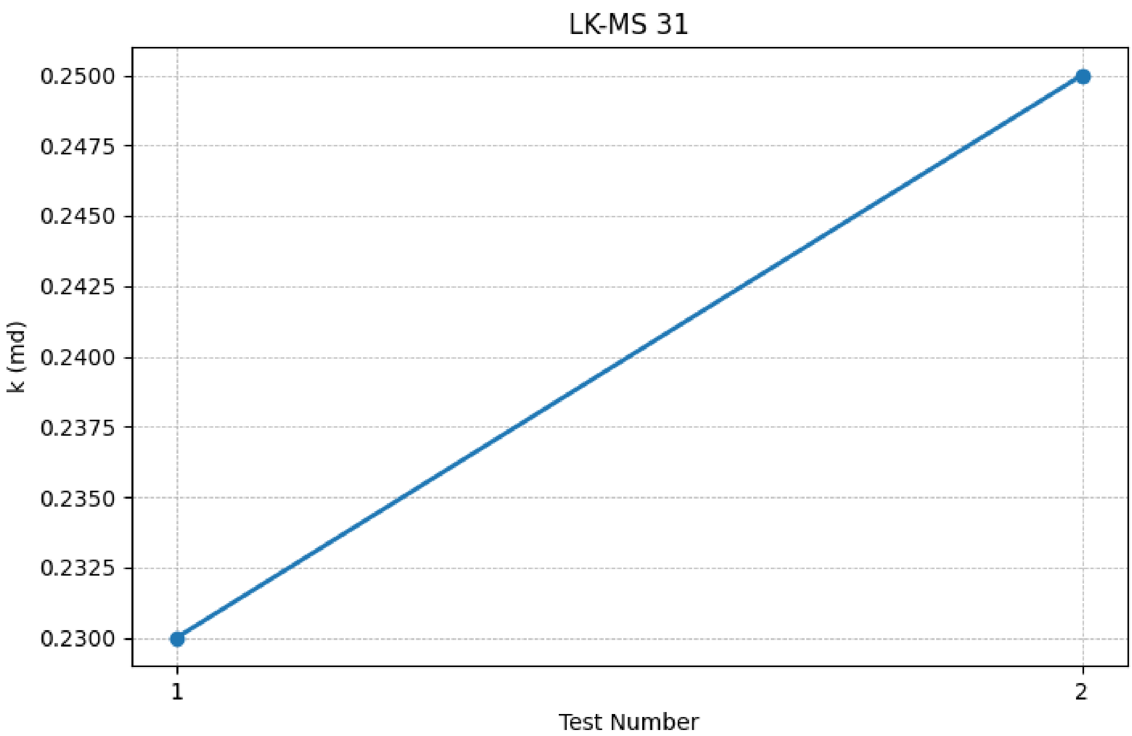

Figure 29: LK-MS 31 permeability results

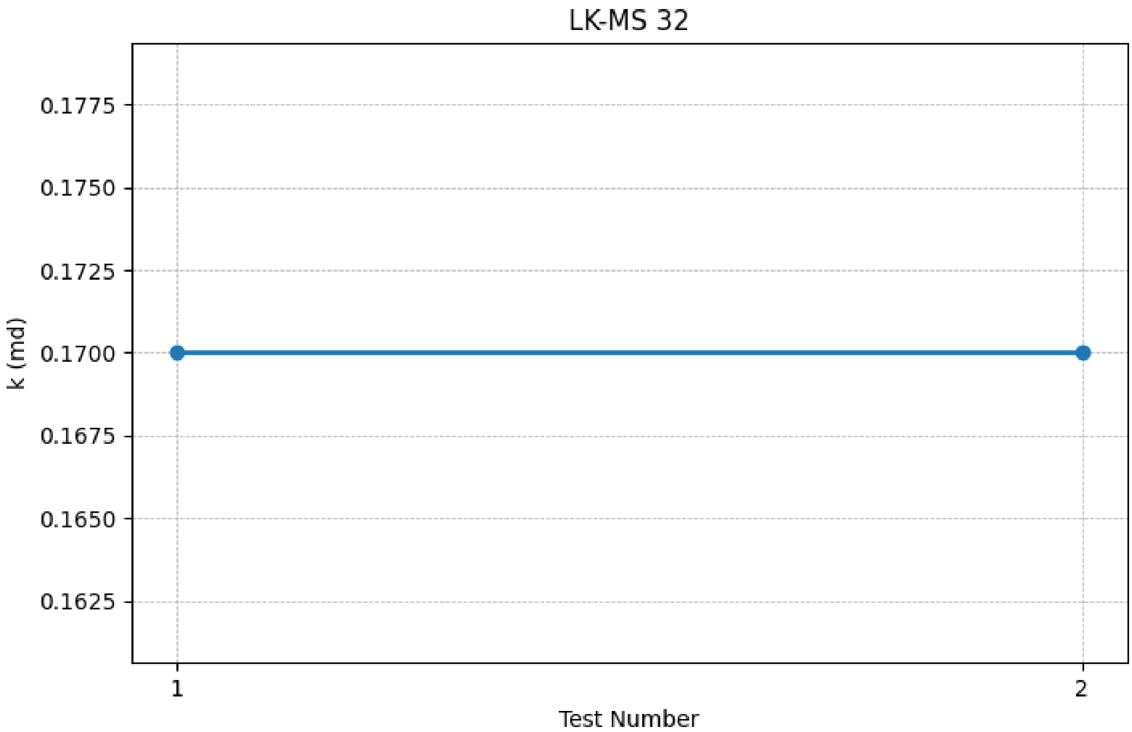

Figure 30: LK-MS 32 permeability results

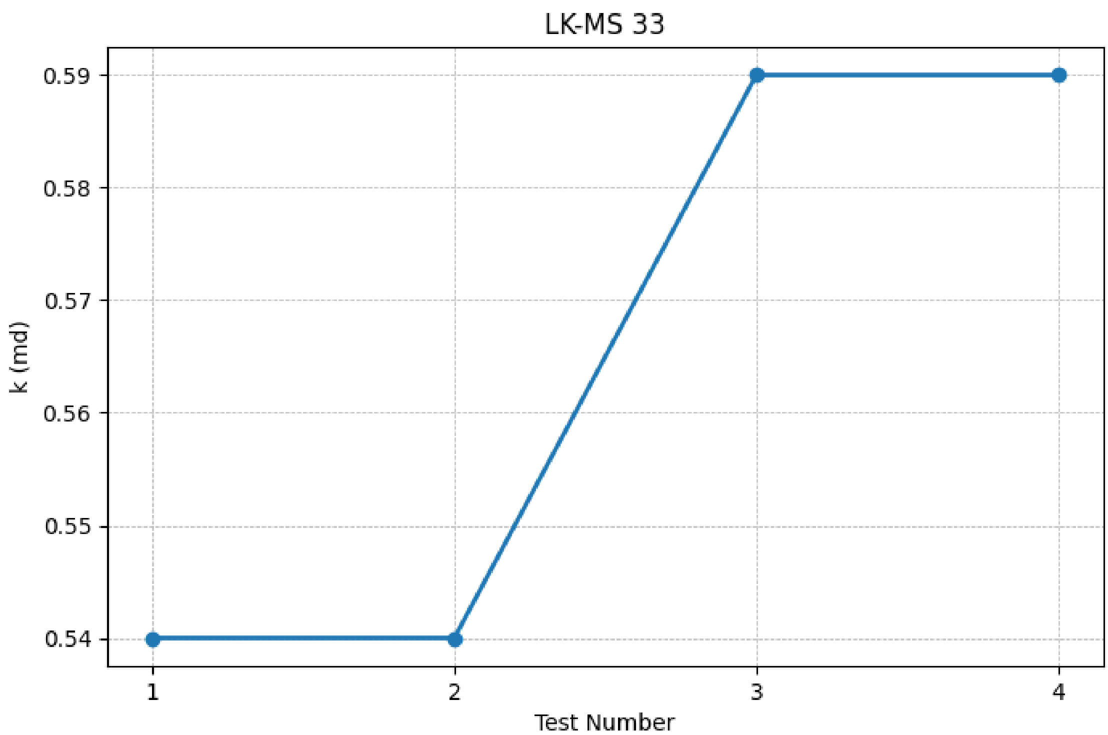

Figure 31: LK-MS 33 permeability results

Sample	Permeability (mD)
LK-MS 5	0.08
LK-MS 7	0.02
LK-MS 8	0.09
LK-MS 11	0.10
LK-MS 12	2.10
LK-MS 15	2.20
LK-MS 18	0.08
LK-MS 19	0.32
LK-MS 20	0.09
LK-MS 22	0.07
LK-MS 24	0.03
LK-MS 25	0.13
LK-MS 29	2.60
LK-MS 30	2.00
LK-MS 31	0.23
LK-MS 32	0.17
LK-MS 33	0.56

Table 5: Permeability measurements of LK-MS samples

17 tests were performed in total, of which 12 tests did not allow for many measurement points due to the low permeability and consequently high infiltration time. 5 tests allowed multiple measurement points. The results of the permeability measurements are visible in table 5.

6.3 Immersion Tests

The following tables are the results of the immersion tests. these have been split into 3 separate tables for each test: md: mass of dry sample, mh: mass of sample under water submerged buoyancy, ms: mass of water saturated sample. MW indicates the average result, and the percent symbol indicates the error between the two measurements.

Probe	md (Dry Mass)			
	24h	48h	MW	%
L1/5	1598,6	1598,9	1598,75	0,02
L1/9	2375,7	2375,4	2375,55	0,01
L1/10	2509,7	2509,4	2509,55	0,01
L13	918,4	918,3	918,35	0,01

Probe	md (Dry Mass)			
	24h	48h	MW	%
L11	1153,4	1153,3	1153,35	0,01
L9/1	640	640	640,00	0,00
L8/2	579,1	579,1	579,10	0,00
L6/10	1438,7	1438,6	1438,65	0,01
L6/1	1077,8	1077,7	1077,75	0,01
LK-MS/5	2439,3	2439,3	2439,30	0,00
LK-MS/7	2524,7	2524,4	2524,55	0,01
LK-MS/8	2269,9	2269,7	2269,80	0,01
LK-MS/11	6655,2	6654,5	6654,85	0,01
LK-MS/12	3279,2	3279	3279,10	0,01
LK-MS/15	2647,4	2647,2	2647,30	0,01
LK-MS/18	2962,9	2960,2	2961,55	0,09
LK-MS/19	2920,4	2920,2	2920,30	0,01
LK-MS/20	4260,5	4260,3	4260,40	0,00
LK-MS/22	4346,7	4346,3	4346,50	0,01
LK-MS/24	4162,2	4162,1	4162,15	0,00
LK-MS/25	2069,3	2069,4	2069,35	0,00
LK-MS/29	3873,2	3872,8	3873,00	0,01
LK-MS/30	3487,3	3487	3487,15	0,01
LK-MS/31	3105,1	3105	3105,05	0,00
LK-MS/32	2311,7	2311,5	2311,60	0,01
LK-MS/33	3710,7	3710,3	3710,50	0,01

Table 6:

Probe	mh (Buoyant Mass)			
	24h	48h	MW	%
L1/5	1035,3	1035,2	1035,25	0,01
L1/9	1532,7	1532,7	1532,70	0,00
L1/10	1600,6	1599,8	1600,20	0,05
L13	595,7	595,3	595,50	0,07
L11	745,6	744,9	745,25	0,09
L9/1	413,3	413,6	413,45	0,07

Probe	mh (Buoyant Mass)			
	24h	48h	MW	%
L8/2	375	375,1	375,05	0,03
L6/10	927,8	928,4	928,10	0,06
L6/1	698	697,8	697,90	0,03
LK-MS/5	1578,8	1580,4	1579,60	0,10
LK-MS/7	1629,6	1631,2	1630,40	0,10
LK-MS/8	1466,2	1465,2	1465,70	0,07
LK-MS/11	4294,7	4294	4294,35	0,02
LK-MS/12	2120,2	2120,4	2120,30	0,01
LK-MS/15	1711,4	1712,9	1712,15	0,09
LK-MS/18	1905,9	1906,8	1906,35	0,05
LK-MS/19	1884,4	1884,2	1884,30	0,01
LK-MS/20	2745,1	2745,6	2745,35	0,02
LK-MS/22	2803,9	2805,8	2804,85	0,07
LK-MS/24	2673,2	2674,2	2673,70	0,04
LK-MS/25	1325,2	1325,1	1325,15	0,01
LK-MS/29	2503	2505,5	2504,25	0,10
LK-MS/30	2259,1	2257,9	2258,50	0,05
LK-MS/31	1998,2	1999,7	1998,95	0,08
LK-MS/32	1487,4	1488,2	1487,80	0,05
LK-MS/33	2389,5	2390,9	2390,20	0,06

Table 7:

Probe	ms (Saturated Mass)			
	24h	48h	MW	%
L1/5	1611,6	1611,8	1611,70	0,01
L1/9	2386,5	2385,7	2386,10	0,03
L1/10	2527,9	2528,3	2528,10	0,02
L13	923,9	924	923,95	0,01
L11	1163,8	1163,2	1163,50	0,05
L9/1	642,7	642,9	642,80	0,03
L8/2	582,2	582,4	582,30	0,03
L6/10	1446,2	1446,5	1446,35	0,02

Probe	ms (Saturated Mass)			
	24h	48h	MW	%
L6/1	1086,3	1086	1086,15	0,03
LK-MS/5	2449,6	2450,3	2449,95	0,03
LK-MS/7	2538,3	2539,2	2538,75	0,04
LK-MS/8	2272,5	2272,5	2272,50	0,00
LK-MS/11	6677,3	6678,6	6677,95	0,02
LK-MS/12	3291	3291,1	3291,05	0,00
LK-MS/15	2656,4	2656	2656,20	0,02
LK-MS/18	2985,5	2986,7	2986,10	0,04
LK-MS/19	2931,7	2932,2	2931,95	0,02
LK-MS/20	4285,8	4286,5	4286,15	0,02
LK-MS/22	4359,8	4359,2	4359,50	0,01
LK-MS/24	4173,3	4175,0	4174,15	0,04
LK-MS/25	2074,0	2074,9	2074,45	0,04
LK-MS/29	3889,2	3891,2	3890,20	0,05
LK-MS/30	3501,3	3502,2	3501,75	0,03
LK-MS/31	3120,1	3119,2	3119,65	0,03
LK-MS/32	2323,8	2323,6	2323,70	0,01
LK-MS/33	3734,8	3734,8	3734,80	0,00

Table 8:

Probe	Density	Porosity
	pb	**p0**
L1/5	2,77	2,25
L1/9	2,78	1,24
L1/10	2,70	2,00
L13	2,80	1,70
L11	2,76	2,43
L9/1	2,79	1,22
L8/2	2,79	1,54
L6/10	2,78	1,49
L6/1	2,78	2,16
LK-MS/5	2,80	1,22

Probe	Density	Porosity
	pb	**p0**
LK-MS/7	2,78	1,56
LK-MS/8	2,81	0,33
LK-MS/11	2,79	0,97
LK-MS/12	2,80	1,02
LK-MS/15	2,80	0,94
LK-MS/18	2,74	2,27
LK-MS/19	2,79	1,11
LK-MS/20	2,77	1,67
LK-MS/22	2,80	0,84
LK-MS/24	2,77	0,80
LK-MS/25	2,76	0,68
LK-MS/29	2,79	1,24
LK-MS/30	2,80	1,17
LK-MS/31	2,77	1,30
LK-MS/32	2,77	1,45
LK-MS/33	2,76	1,81

Table 9:

6.4 Porosity and Permability Tests from Gas Permeameter

The following results (Fig 26) are from the gas permeability tests showing the Klinkenberg permeability (Kd). Many of the results had a permeability that was too low to warrant any repeat tests under confining pressure, as this would have taken a great amount of time for unnecessary results. The permeability results show wide variation from as low as 0.0005mD to 5.5mD. Six results showed high enough permeability for confining pressure tests, two of which were unusable due to a critical error with the equipment resulting in deformed samples that cannot be reused. The avergate permeability reduction was measured at about 95% based on results with a pressure of greater than 4500 psi (Table 10).

Porosity also shows a strong decrease with pressure with samples typically loosing about 72.86% of their porosity based on the results that had a pressure of greater than 4500 psi (Table 11).

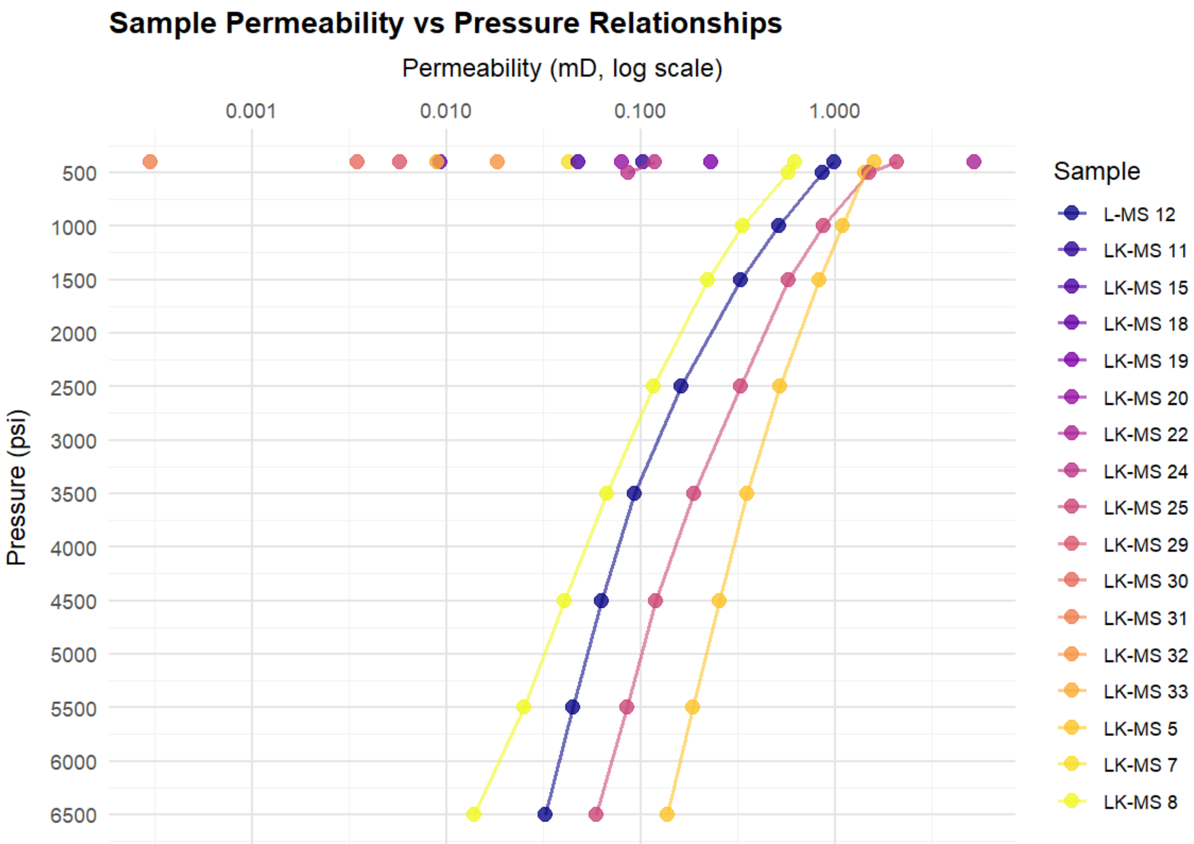

Figure 32: Diagram showing permeability through pressure. Pressure given in PSI, Permeability given in mD.

Sample	Start Permeability (400 psi)	End Permeability	Max PSI	Permeability Reduction (%)
LK-MS 5	1.6011	0.1372	6500	91.43%
LK-MS 7	0.0425	N/A	400	No result
LK-MS 8	0.6187	0.0139	6500	97.75%
LK-MS 11	0.1035	N/A	400	No result
LK-MS 12	0.9866	0.0322	6500	96.73%
LK-MS 15	0.0479	N/A	400	No result
LK-MS 18	0.0093	N/A	400	No result
LK-MS 19	0.2299	N/A	1500	No result
LK-MS 20	0.0802	N/A	400	No result
LK-MS 22	5.2393	0.9193	4500	82.45%
LK-MS 24	0.1178	0.0859	500	27.12%
LK-MS 25	2.0942	0.0589	6500	97.19%
LK-MS 29	0.0058	N/A	400	No result
LK-MS 30	0.0035	N/A	400	No result
LK-MS 31	2.79E-04	N/A	400	No result
LK-MS 32	0.0183	N/A	400	No result
LK-MS 33	0.0090	N/A	400	No result

Table 10: Permeability reduction summary for samples at different confining pressures.

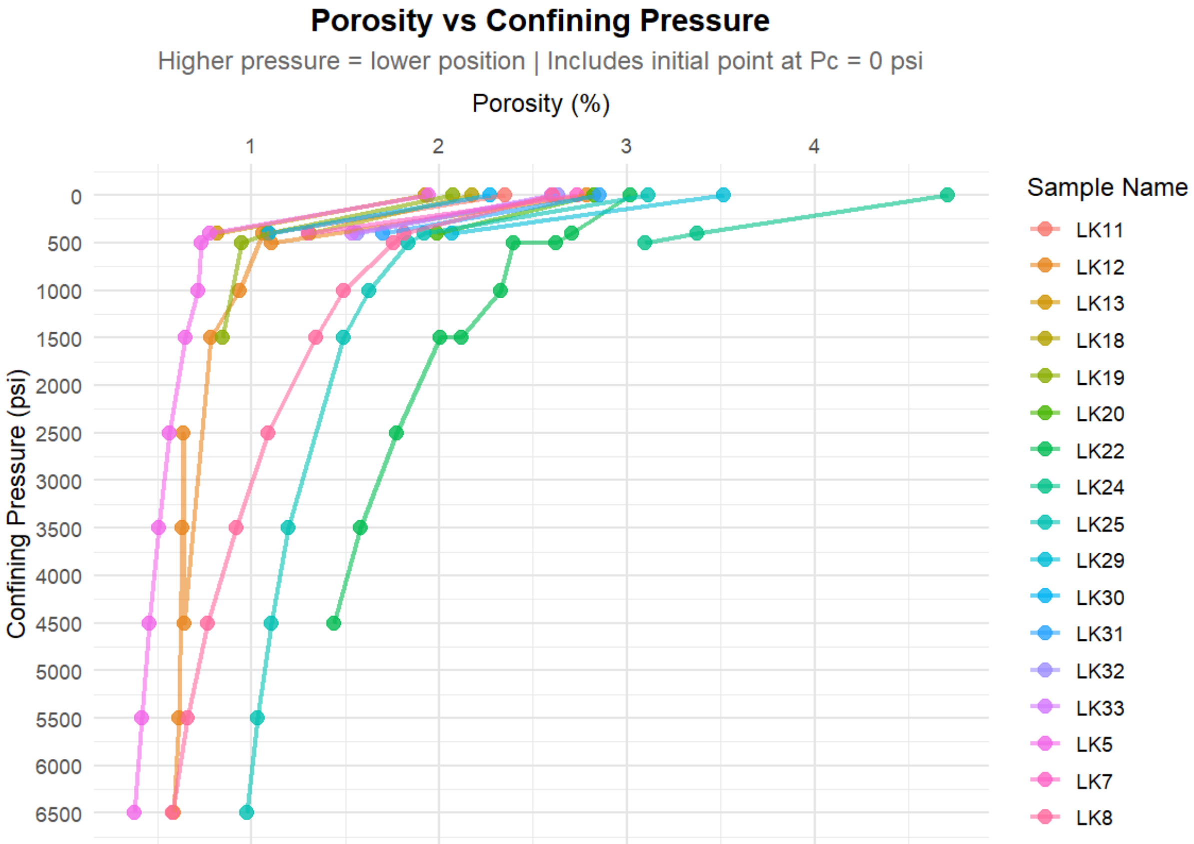

Figure 33: Diagram showing porosity through pressure. Pressure given in PSI, Porosity given in %.

Sample	Start Porosity (Vp0)	End Porosity	Max PSI	Porosity Reduction (%)
LK-MS 5	1.9451	0.3801	6500	80.46%
LK-MS 7	2.7344	1.3026	400	52.36%
LK-MS 8	2.6038	0.5804	6500	77.71%
LK-MS 11	2.3515	1.0822	400	53.98%
LK-MS 12	3.8757	0.5852	6500	84.90%
LK-MS 15	1.9274	0.8204	400	57.44%
LK-MS 18	2.1755	1.3084	400	39.85%
LK-MS 19	2.0792	0.8484	1500	59.19%
LK-MS 20	2.8276	1.9905	400	29.61%
LK-MS 22	3.0503	1.4382	4500	52.85%
LK-MS 24	4.7649	3.0998	500	34.94%
LK-MS 25	3.0966	0.9789	6500	68.39%
LK-MS 29	3.5187	2.0657	400	41.29%
LK-MS 30	2.2700	1.0930	400	51.85%
LK-MS 31	1.6359	2.8544	400	-74.48%
LK-MS 32	2.6329	1.5648	400	40.57%
LK-MS 33	2.6007	1.5347	400	40.99%

Table 11: Porosity reduction summary for samples at different confining pressures.

7 Discussion

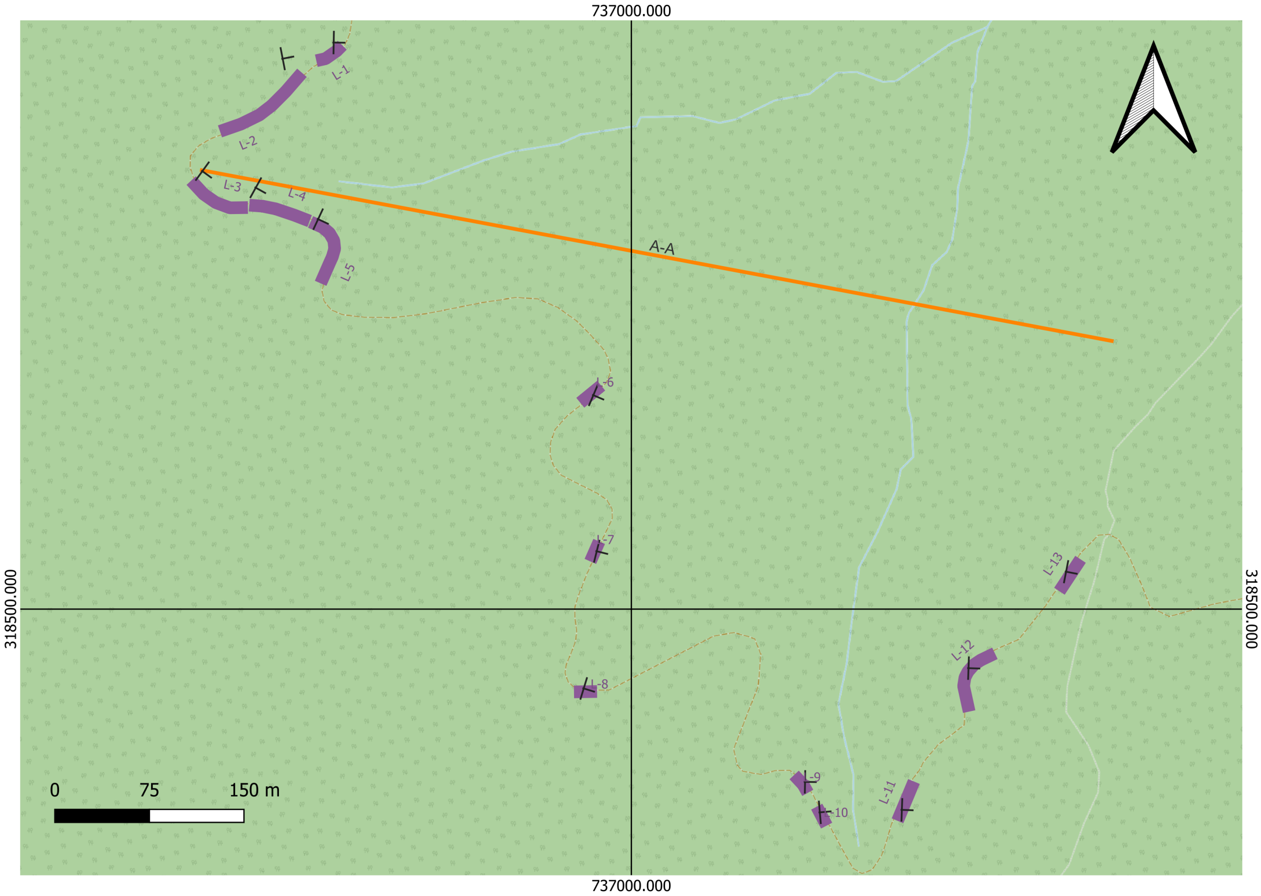

Figure 34: Map showing non-averaged bedding direction

7.1 Dolomite Thickness Analysis

One of the primary objectives of the study in this area was to determine the minimum thickness of the dolomite that was analyzed. To this end the measured dolomite outcrop banks were summed up to provide thicknesses for the outcrops themselves; however, this was insufficient as the route covered a large length, often with extremely large gaps between outcrops. A second problem that occurred was the fact that GPS measurements taken on site were not accurate enough to perform a purely mathematical reconstruction based on absolute height and length of the outcrops together. Such a method would require the use of precise GPS instrumentation.

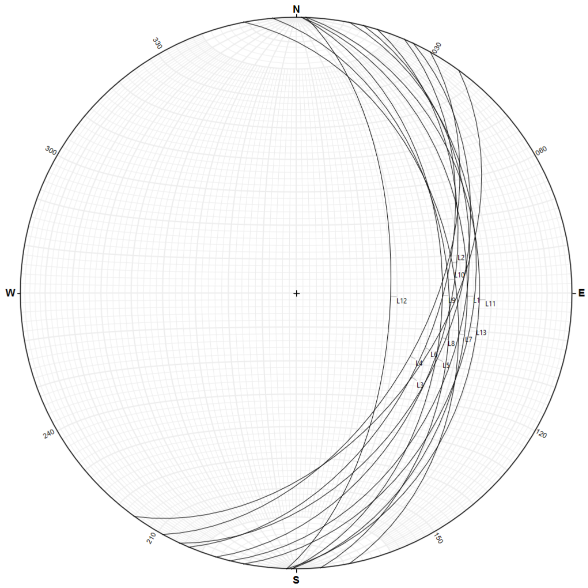

Figure 35: Stereoplot showing measured bedding angles

The solution chosen was to reconstruct the profile along a section line (Fig. 34, 36 Section A-A) that was orientated to the average dip direction of all collected bedding data (Fig. 35). The dip and dip direction were first averaged to a single value that was applied to all points resulting in a dip direction/dip of 101/44. The strikes were projected onto the section line and their length along the section line was noted along with their absolute height (Table 7). The length of the section line is approximately 730 m.

The section line was measured at approximately 750m long, and the strike lines of each outcrop intersect the section line at specific intervals and heights. These were collected and plotted in a graphical design program to fully reconstruct the profile and provide the approximate total thickness of this area, including the gaps.

The resulting section (Fig. 37) shows an approximate total thickness of 510 meters. This thickness can be used as an absolute minimum value for any reservoir calculations that involve these dolomite series, although it is important to remember that this section only accounts for the visible outcrops. Of the 510m calculated thickness, approximately 24% is visible.

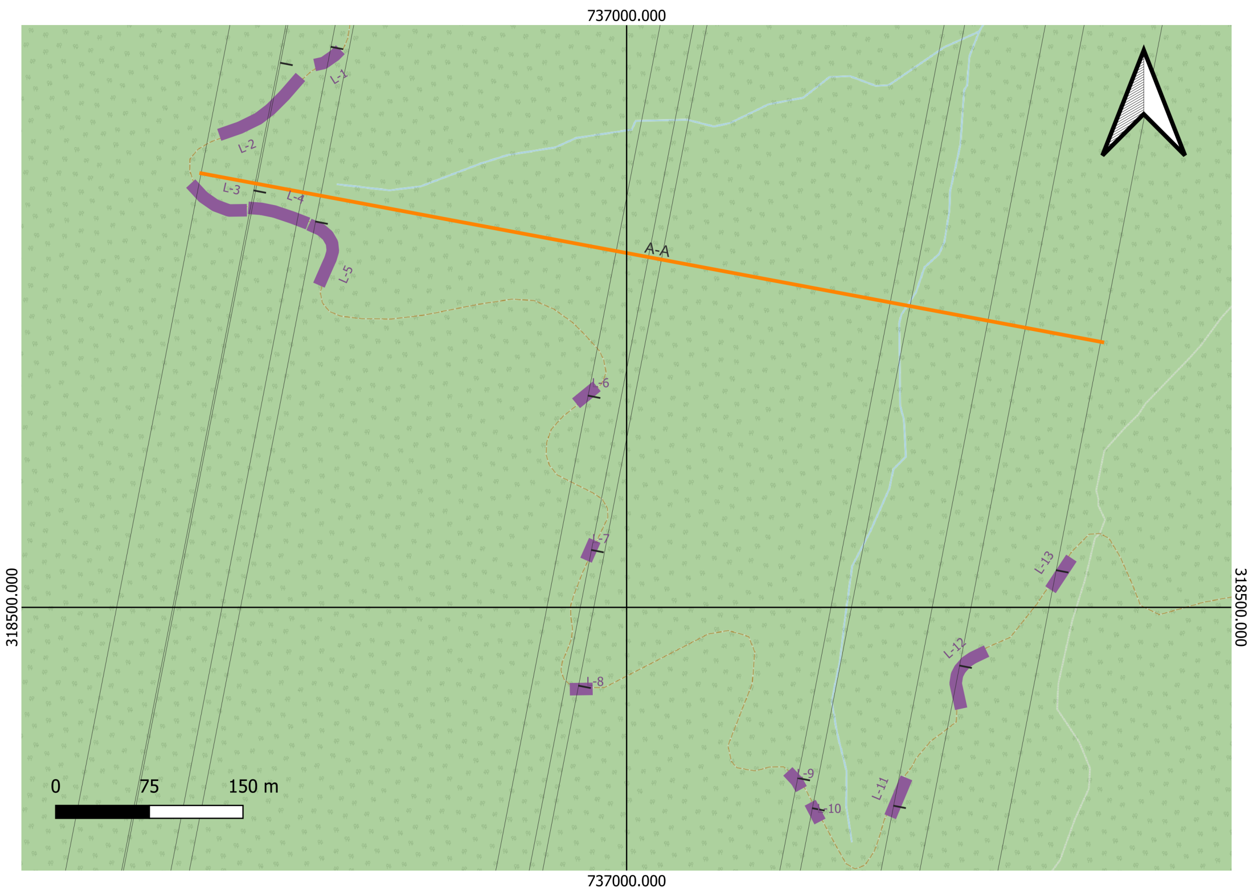

Figure 36: Section line showing dip intersections from the average dip direction

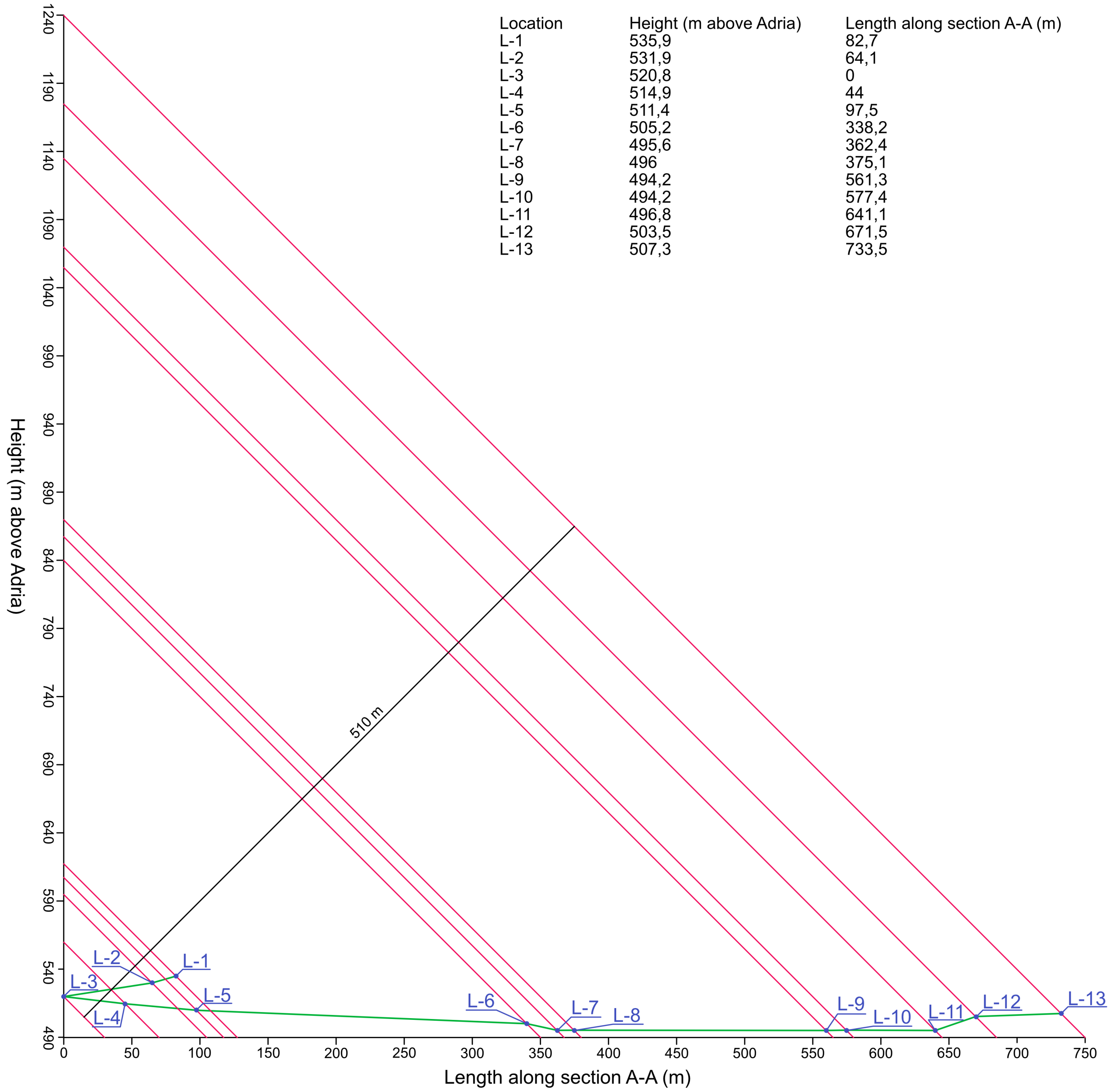

Figure 37: Diagram showing approximate total thickness of the measured outcrops. Green line shows the approximate route of the forest road with the position of each outcrop marked along it

7.2 Slug Test Analysis

The results from the constant head slug tests show highly variable permeability at the matrix and microfracture scale of the host rock. This variability can be attributed to the strong differences in fracture density, mineralization, and porosity of the unit being tested. These results give us the absolute minimum permeability that can be expected, however encountering such permeability is highly unlikely due to the highly fractured nature of the rock mass in general at larger scales; during drilling more than 50 percent of all attempts failed due to the presence of large fractures deeper in the rock wall, which then give invalid results as any water immediately flows in to these fractures, rather than the micro-fractures

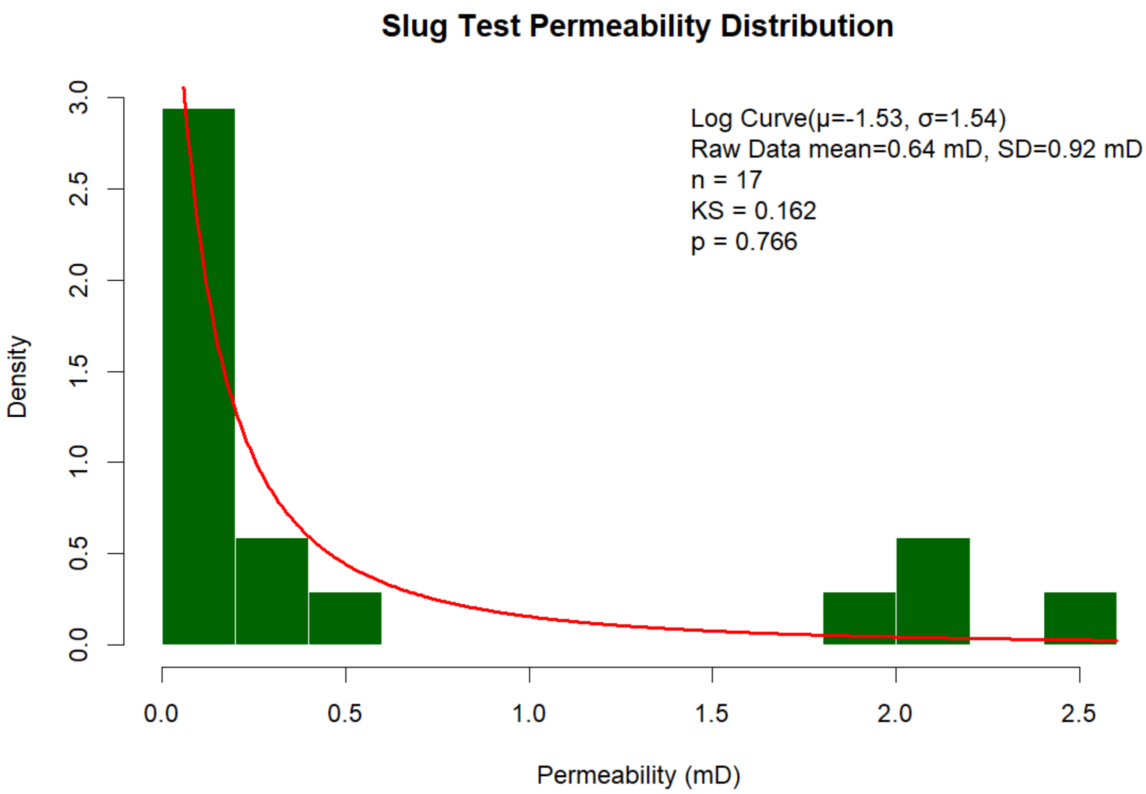

Figure 38: Histogram and fitted log-normal distribution curve of constant-head slug tests in milliDarcy. Fitted log normal curve is used later to determine possible outputs of pumping tests

and pores that are desired. The presence of these large fractures is rather ubiquitous, the result being an expected permeability much higher than those shown in the slug test and permeameter tests.

The results were plotted as a histogram. Several distribution types against this histogram were tested, and it was found to follow the log-normal distribution type (Fig. 38). To test suitability of fit, a Kolmogorov-Smirnov test was applied to the fit, with a resulting P-value of 0.766 indicating a good fit. This was also the best fit of all tested distribution models.

7.3 Permeameter Analysis

The results of the permeameter tests were collected into a permeability distribution in order to compare it with the slug test distribution. The gas permeability results show much higher permeability for the samples, but this could be attributed to the limitations of the Klinkenberg correction formula, unforseeable problems with the mini-slug test process, such as some pores and fractures becoming slightly sealed with dust as it is drilled, or simply the fact that the plugs are too small for a proper volumetric representation of the rock mass. Figure 39 shows the distribution of the Klinkenberg gas permeability measurements. Although as described previously they display generally higher permeaility than the mini-slug tests, they still follow the same normal distribution. The Kolmogorov Statistic is less ideal also in this distribution as we also have two distributions at work within the results; one for the matrix permeability, and one for the fracture permeability.

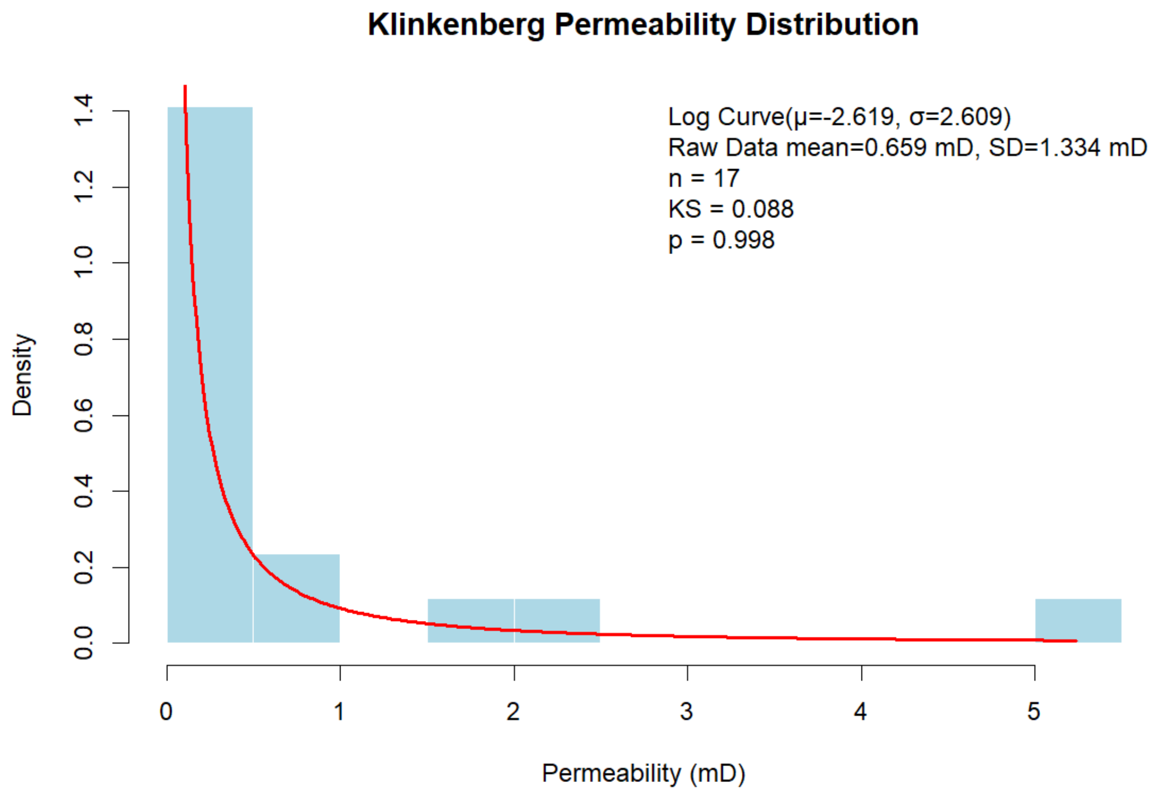

Figure 39: Histogram and fitted log-normal distribution curve of Klinkenberg permeability tests in milliDarcy. Fitted log normal curve is used later to determine possible outputs of pumping tests

7.4 Immersion Test Analysis

The results from the immersion test allowed the creation of distribution diagrams for both the density and porosity of the samples. The density shows a mean of 2.78 g / cm3, with a very tight standard deviation of 0.02 + / - (Fig. 40). This density is in line with the global measurements of Dolomite, although more towards the lower end with dolomite having typical density ranges of 2.8 - 2.9 g/cm3, with a global average of 2.84g/cm3 [Webmineral.com,]. This could be due to the heavy recrystalization with calcite in the porespaces and fractures, as well as from the pore space itself. The porosity percentage distribution is more normal, with a mean of 1.46 percent, and a standard deviation of 0.57 percent (Fig. 41).

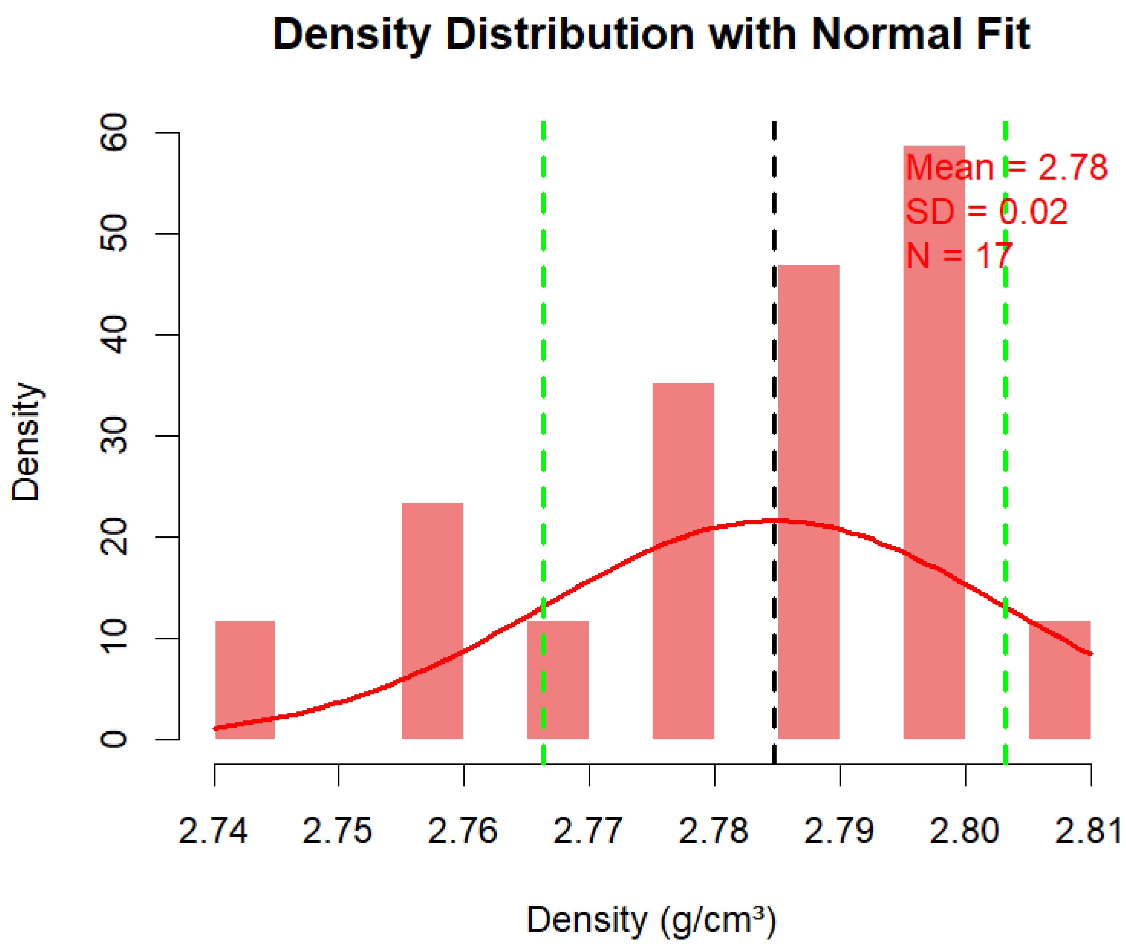

Figure 40: Density distribution of immersion tests showing very tight distribution

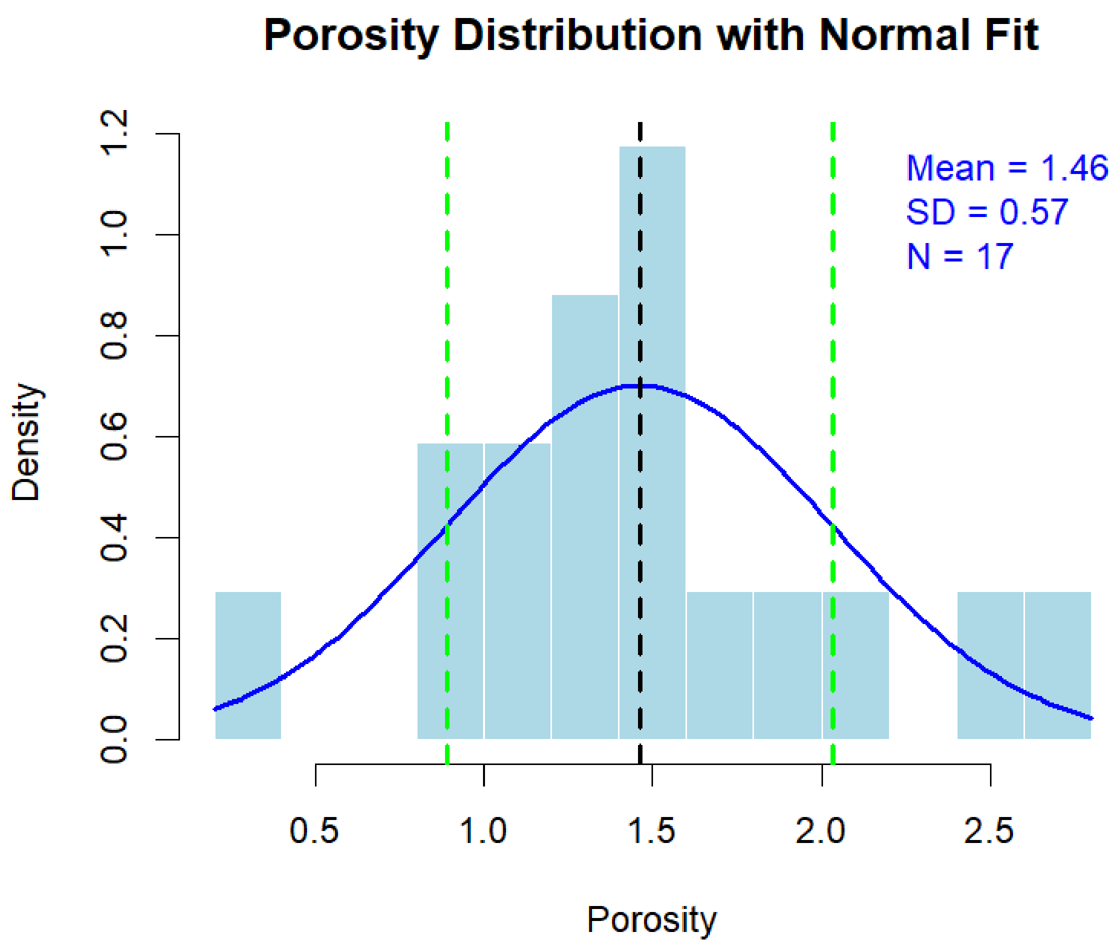

Figure 41: Distribution diagram of sample porosity from immersion tests

7.5 Permeability/Porosity

The permeability/Porosity measurements for each method (Klingenberg, and mini-slug test/ immersion) were plotted together to see how these methods deviated from one another, and if any correlations were visible (Fig. 42)

The slug/immersion method shows a much tighter grouping than the gas permeability results, possibly due to the Klinkenberg correction factor again. The gas permeameter also seems to estimate porosity higher than the immersion method, the reason for this is unknown. There are also several anomalies within the gas measurements, which can be attributed to errors in the machine that can be corrected in future. When looking for a correlation there is indeed a slight relationship between porosity and permeability. The trend lines are slightly positive on the Log scale, indicating that as porosity increases, so does the permeability. What is interesting to note here is that both sets of results are quite similar, just shifted left/right slightly, with the calculated trendlines remaining the same, which would suggest that both methods are equally viable for determining the permeability, but with the possible explaination that the gas porosimetry samples very small pores which are not filled during the immersion test.

Figure 43 shows how the results of each permeability analysis match up with each other. Major outliers of the Klinkenberg permeability can be attributed to the presence of larger fractures within the plug samples.

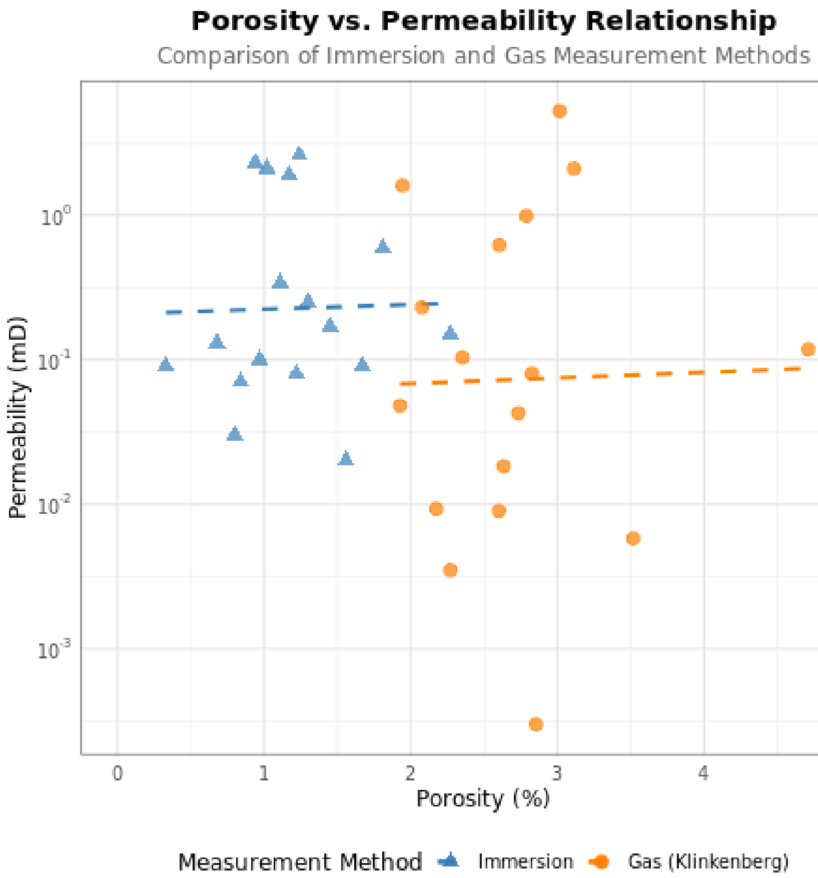

Figure 42: Comparison between immersion/slugtest method and Klinkenberg porosity/permeability. Porosity values for the blue points are taken from the immersion method, and permeability is taken from slugtests, for the orange points both porosity and permeability values are taken from the Vinci permeameter results.

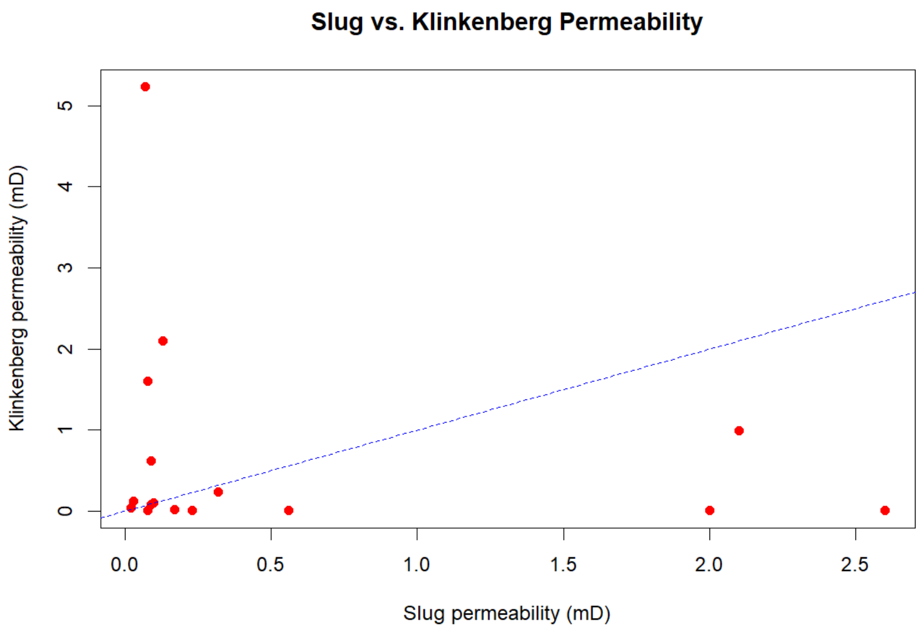

Figure 43: Scatterplot showing the Slug permeability vs Klinkenberg permeability

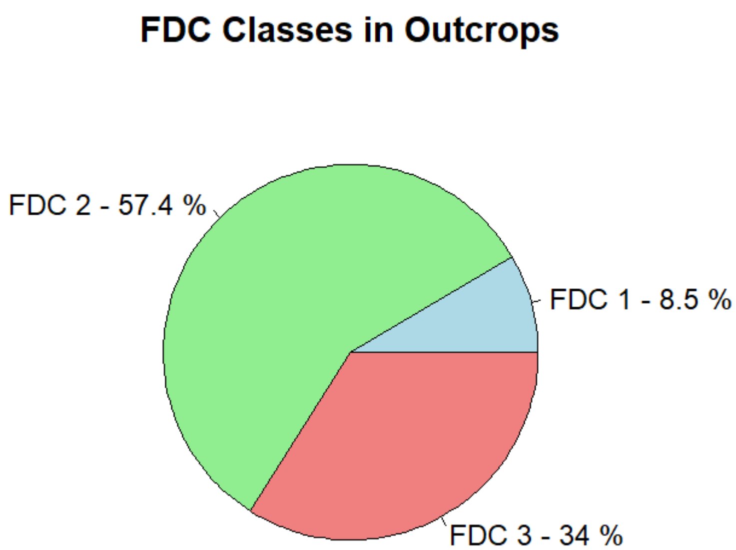

Figure 44: Pie chart showing the frequency of FDC classes within the entire outcrop

7.6 Fracture Density Class

The outcrop shows a large abundance of FDC 2 class fractures (Fig. 44) with many FDC 3, and a small amount of FDC 4. this provides a good level of fracturing for potential reservoir flow as the majority of fractures are closely spaced, with few being poorly fractured. This fracture frequency was correlated with the measured permeabilities and porosities from the slug tests and immersion tests (Fig. 45) When looking at the permeabilities we do indeed see a correlation, with permeability increasing with FDC. This is in line with expectations as higher FDC classes indicate higher fracture densities and thus higher permeabilities. The diagram also shows how the porosity does not necessarily correlate with the FDC, with the higher porosities being located within FDC 2 class samples. This would indicate that the most important aspect for permeability is the presence of fractures, with the pore space being of less importance perhaps due to the presence of unconnected pore space. The average permeabilities for each FDC are as follows:

- FDC 1: Average permeability = 0.095 mD
- FDC 2: Average permeability = 0.395 mD
- FDC 3: Average permeability = 1.190 mD

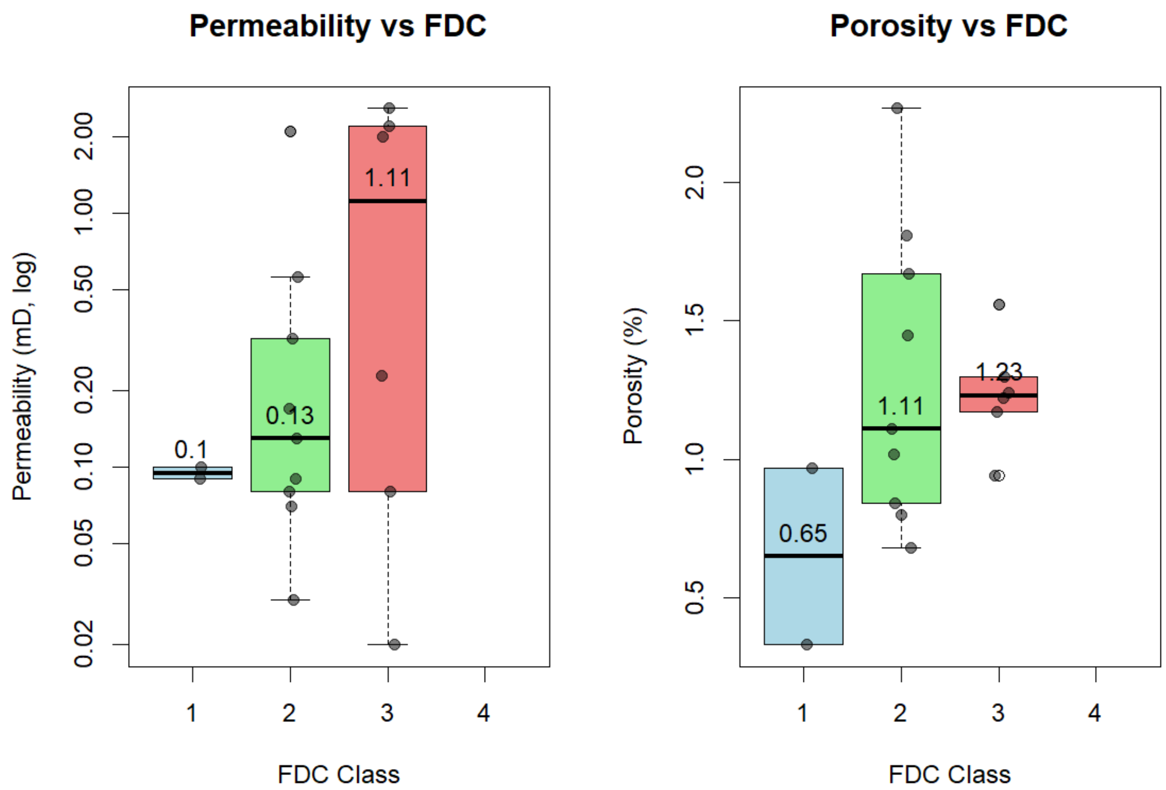

Figure 45: Correlation of FDC with permeability of slug tests. Tails show max data range, upper and lower box limits show 25th and 75th percentile, black line with value shows median value.

Sample	Slug Permeability (mD)	Porosity (Immersion, %)	FDC
LK-MS 5	0.08	1.22	3
LK-MS 7	0.02	1.56	3
LK-MS 8	0.09	0.33	1
LK-MS 11	0.10	0.97	1
LK-MS 12	2.10	1.02	2
LK-MS 15	2.20	0.94	3
LK-MS 18	0.08	2.27	2
LK-MS 19	0.32	1.11	2
LK-MS 20	0.09	1.67	2
LK-MS 22	0.07	0.84	2
LK-MS 24	0.03	0.80	2
LK-MS 25	0.13	0.68	2
LK-MS 29	2.60	1.24	3
LK-MS 30	2.00	1.17	3
LK-MS 31	0.23	1.30	3

LK-MS 32	0.17	1.45	2
LK-MS 33	0.56	1.81	2

Table 12: Slug permeability, Porosity (Immersion), and FDC values for each sample.

7.7 Flow Estimation

To determine the flow rate, a modified version of the Dupuit-Thiem formula was used (Equation 13, [Bouwer and Rice, 1976]), with the Darcy K_f equation (Equation 14, [Bear, 1972]), and the R_e equation (Equation 15, [Vasvari, 2001]).

$$Q = (2\pi K_f L) \cdot \frac{y}{\ln\left(\frac{R_e}{r_w}\right)} \tag{13}$$

$$K_f = \frac{kg\rho}{\mu} \tag{14}$$

$$R_e = 3000\, L\sqrt{K_f} \tag{15}$$

Where:

- Q : Flow (m^3/day)
- K_f : Hydraulic conductivity (m/s)
- L : Length of the section of well through which water enters (m)
- y : Drawdown (m)
- R_e : Effective radius over which y is dissipated (m)
- r_w : Well radius (m)
- μ : Dynamic viscosity of water (Pa·s)
- ρ : Density of water (kg/m^3)
- g : Acceleration due to gravity (m/s^2)
- k : Intrinsic permeability of the aquifer (m^2)

Parameter	Unit	Value
Well Radius	m	0.12
Water Density	kg/m^3	971.32
Water Dynamic Viscosity	Pa·s	0.0002
Length of Section	m	510
Gravity	m/s^2	9.81

Table 13: Table showing assumed values for the Dupuit-Thiem calculations

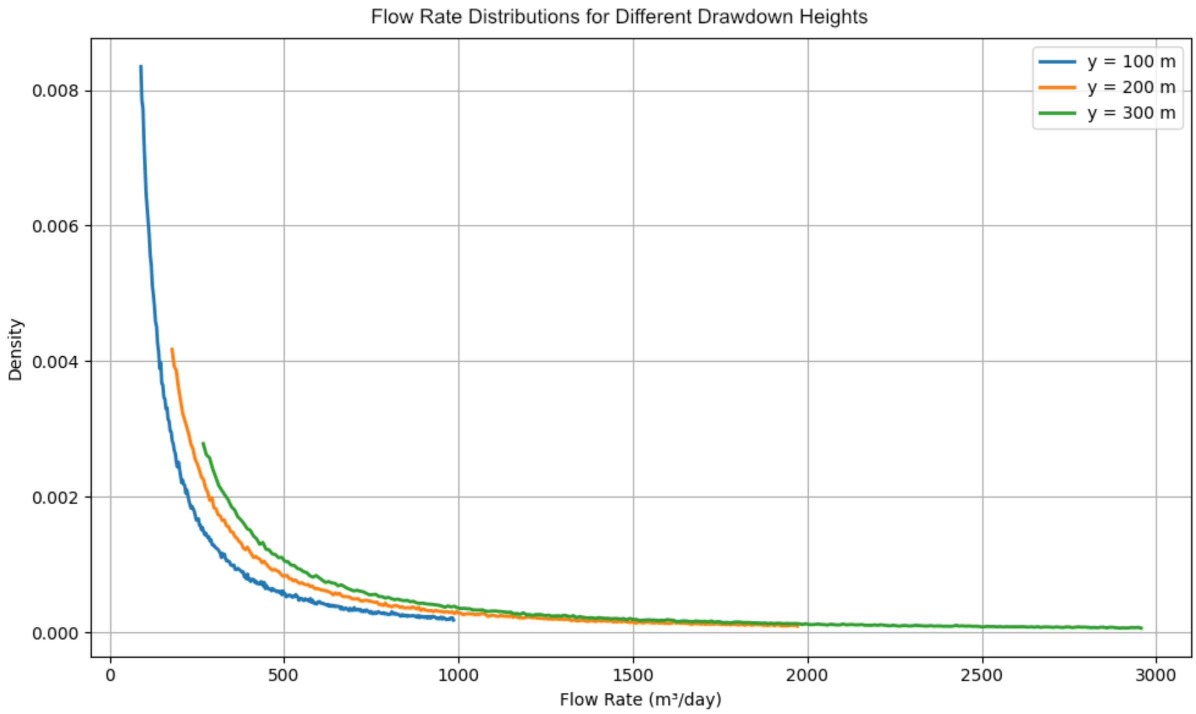

Figure 46: Monte-Carlo distributed flow rates for different drawdowns

Several assumptions must also be made for certain values by using values taken from an internal EVN project (Table 13).

The Drawdown has been calculated for 3 different values: 100m, 200m, 300m.

We can make an estimate of R_e as the radius of influence is an unknown, but can be approximated by Equation 15 [Vasvari, 2001]

A Monte-Carlo simulation for each drawdown variable was run on the permeability distribution determined earlier (Fig. 38), which was found to have a log normal distribution with a Lambda value of -1.53 and a k minimum of 0.2 mD, and a maximum of 2.6 mD (Fig. 46).

Using this distribution, we can then calculate the cumulative distribution for each drawdown, and plot their P50 values (Fig. 47).

These P50 values equate to 100000 (y = 100m), 200000 (y = 200m), and 300000 (y = 300m) Litres of water per day, and assuming that the dolomite series is 510m thick, which is a reasonable assumption.

It must be noted however that these values were taken at surface level using the slug permeability values, as there were too few confined gas permeability values to run the simulation.

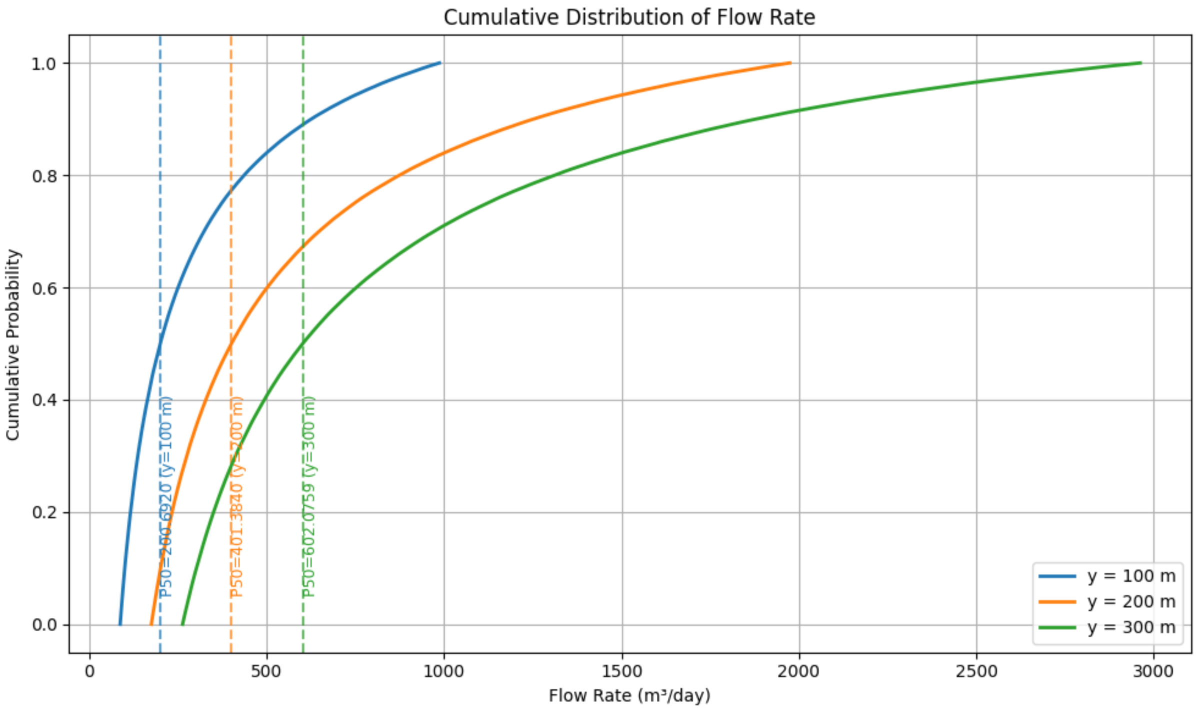

Figure 47: Cumulative flow calculations for each drawndown, including P50 values

8 Conclusion

During this thesis the base reservoir permeability characteristics of the Ramminger Dolomite series on the Hohe Lindkogel near Baden were determined using various methods; In situ constant-head mini slug tests, gas permeability measurements using samples from the same slug test locations, and bedding measurements over the length of the outcrop. After analysing and comparing the results the following conclusions were reached:

- Slug test permeabilities show a distinctive log-normal distribution for the lower permeabilities, however a second distribution was identified for the higher permeabilities following a normal distribution. This indicates that the log-normal distribution applies to the matrix permeability of the rock, where no microfractures are present, or are completely sealed, and the normal distribution applies to rock masses with microfractures that are open. This also explains the wide variation in measured permeabilities. More measurements would have to be collected in order to fully confirm this conclusion.

- The gas permeability results typically show higher permeabilies than the slug tests. This could be due to several factors such as slight sealing of the slug test drill hole during drilling reducing permeability, or slight opening of the fractures in the plug samples during heavy coring. These samples nevertheless also show similar distributions as with the slug tests.

- The bedding measurement results enabled a reconstruction of the unit thickness based on the outcrop that was visible. This reconstructions showed a thickness of about 510 meters, however the unit is much bigger than this. When this is considered next to the high failure rate of slug test drill holes as a result of large fractures present in the rock indicate that the level of fracturing is extremely high throughout the whole series, and that the actual permeability is much higher than what was measured in this study, we can conclude that the formation is well suited to geothermal use, particularly as these units are also present at depths where temperatures are sufficient.

A stratigraphic diagram was created by extrapolating the positions from the thickness diagram (Fig. 37) as a final reference for all measurements taken (Fig. 48). Two detailed diagrams of all outcrops are available as Figs. 49 & 50, which show the individual bedding layouts.

Additionally, a Monte-Carlo simulation was conducted for the slug test permeability distributions at surface level, for 3 different values of drawdown, which showed strong response despite the low permeability as a result of the 510m aquifer thickness.

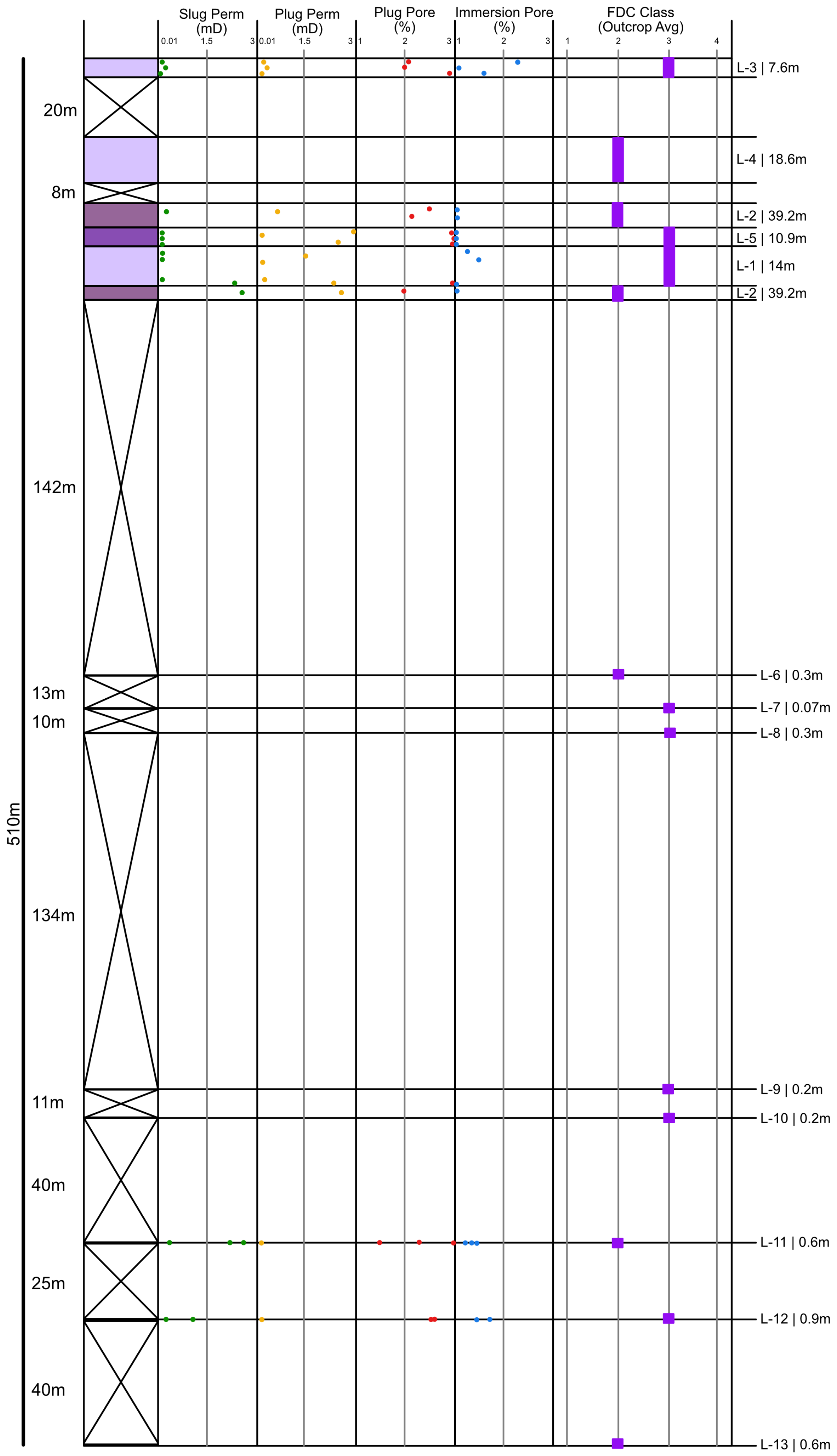

Figure 48: Stratigraphic Pile of the Lindkogel outcrops extrapolated from Fig. 37. Includes all permeability and porosity measurements with average FDC for each outcrop. Note: Outcrops 1 and 5 are overlain on outcrop 2

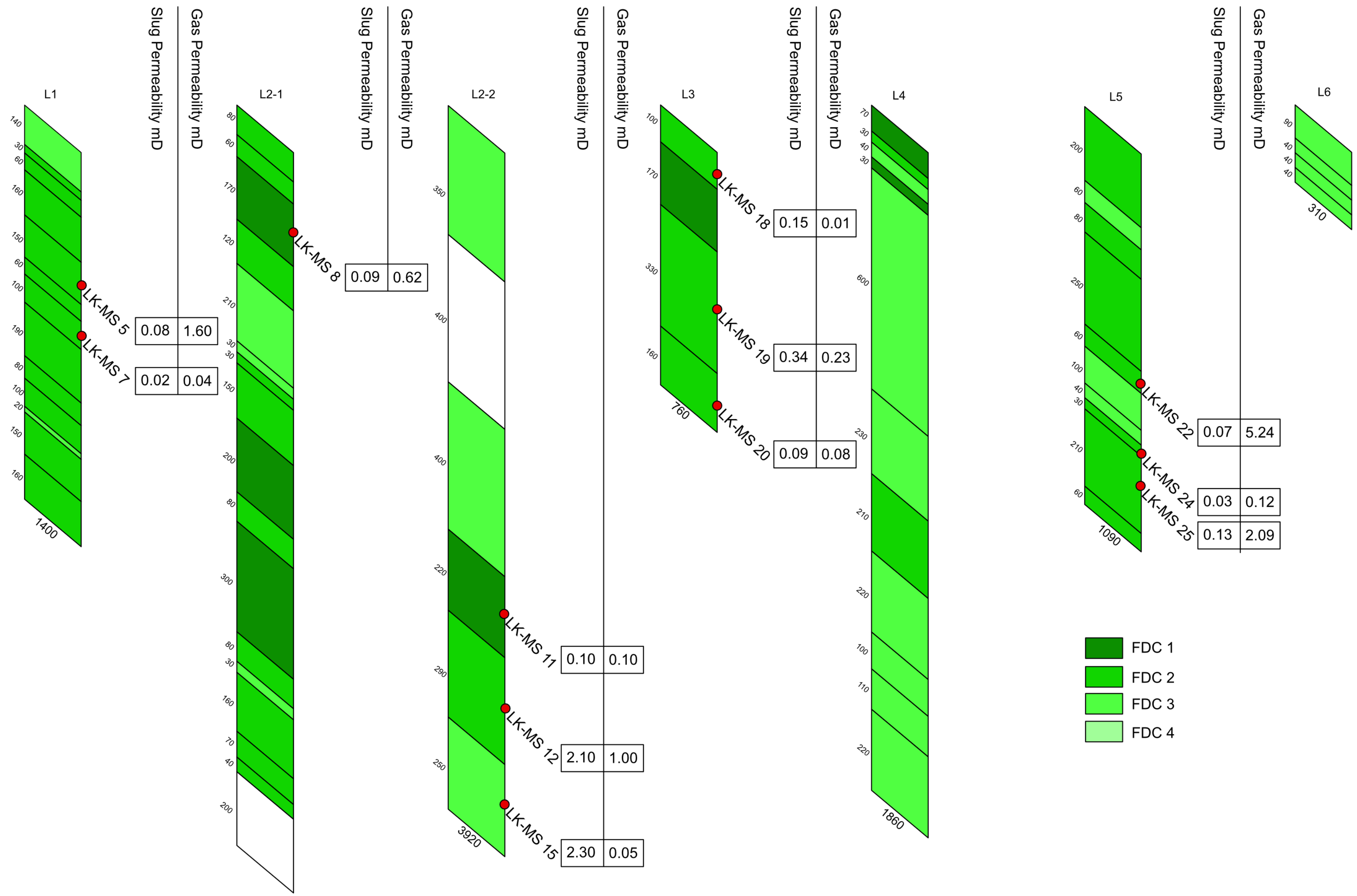

Figure 49: L1-L6 diagram showing thickness of all beds and total unit thickness (in cm). Also shown are the slug test permeability, and gas permeability results (in mD).

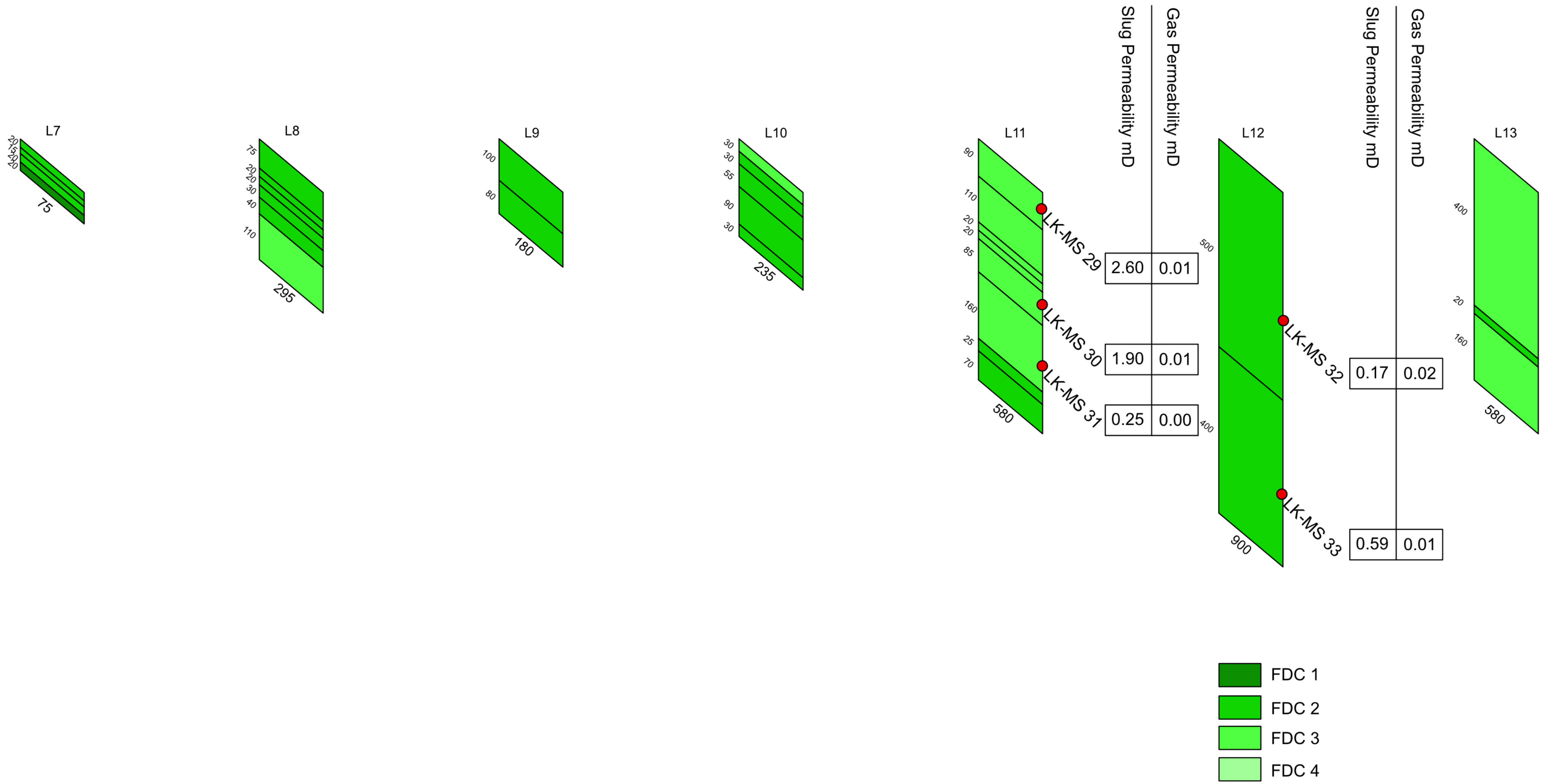

Figure 50: L7-L13 diagram showing thickness of all beds and total unit thickness (in cm). Also shown are the slug test permeability, and gas permeability results (in mD).

9 References

[Bear, 1972] Bear, J. (1972). *Dynamics of Fluids in Porous Media.* Elsevier, New York.

[Bouwer and Rice, 1976] Bouwer, H. and Rice, R. C. (1976). A slug test method for determining hydraulic conductivity of unconfined aquifers with completely or partially penetrating wells. *Water Resources Research*, 12(3):423–428.

[Curewitz and Karson, 1997] Curewitz, D. and Karson, J. A. (1997). Structural settings of hydrothermal outflow: Fracture permeability maintained by fault propagation and interaction. *Journal of Volcanology and Geothermal Research*, 79(3–4):149–168.

[Decker, 2007] Decker, K. (2007). Dolomite fracture and fault analysis, outcrop study steinbruch gaaden. Unpublished report, OMV Austria, Vienna.

[Doglioni and Ferrara Bosellini, 1987] Doglioni, C. and Ferrara Bosellini, E. (1987). Eoalpine and mesoalpine tectonics in the southern alps. *Geologische Rundschau*, 76:735–754.

[Faupl, 2000] Faupl, P. (2000). *Historische Geologie.* Wien Facultas, Vienna.

[Fruth and Scherreiks, 1982] Fruth, I. and Scherreiks, R. (1982). Hauptdolomit (norian) — stratigraphy, paleogeography and diagenesis. *Sedimentary Geology*, 32:195–231.

[Henrich and Zankl, 1986] Henrich, R. and Zankl, H. (1986). Diagenesis of upper triassic wetterstein reefs of the bavarian alps. *Reef Diagenesis.*

[Hölting and Coldewey, 2013] Hölting, B. and Coldewey, W. G. (2013). *Hydrogeologie: Einführung in die Allgemeine und Angewandte Hydrogeologie.* Spektrum Akademischer Verlag, Heidelberg, 8 edition.

[Kázmér, 1990] Kázmér, M. (1990). Birth, life and death of the pannonian lake. *Palaeogeography, Palaeoclimatology, Palaeoecology*, 79:171–188.

[Leitner and Spötl, 2017] Leitner, C. and Spötl, C. (2017). Multistage development of extremely deformed evaporites. In Soto, J. I., Flinch, J., and Tari, G., editors, *Permo-Triassic Salt Provinces of Europe, North Africa and the Atlantic Margins: Tectonics and Hydrocarbon Potential.* Elsevier, Amsterdam.

[Mandl, Gerhard W., 1999] Mandl, Gerhard W. (1999). Field trip guide – foregs '99 vienna – dachstein–hallstatt–salzkammergut region. Technical Report 49, Geologische Bundesanstalt, Vienna. ISSN 1017-8880; 43 figures; contributions by various authors including Wessely, Piller, Hofmann.

[Moser, 2023] Moser, M. (2023). Bericht 2023 über geologische, stratigrafische und mikrofazielle untersuchungen in der mitteltrias-schichtfolge des hohen lindkogel, 834 m, bei baden (Ök 58 badem) und des harzberges, 466 m, bei bad vöslau (Ök 76 wiener neustadt). https://opac.geologie.ac.at/ais312/dokumente/Bericht Accessed: 31 Aug 2025.

[Penz-Wolfmayr et al., 2022] Penz-Wolfmayr, M., Bauer, H., Rupprecht, D., and Decker, K. (2022). Analyse von aufschlussäquivalenten der speichergesteine – hauptdolomit formation. Unveröffentlichter bericht, Universität Wien / WienEnergie, Vienna.

[Pirmoradi, 2022] Pirmoradi, R. (2022). Hydraulic conductivity of fault zones in fractured carbonate rocks (case study: Hochschwab, austria). Master's thesis, University of [insert university name]. In partial fulfillment of the requirements for the degree of Master of Science (MSc).

[Sibson, 1996] Sibson, R. H. (1996). Structural permeability of fluid-driven fault-fracture meshes. *Journal of Structural Geology*, 18(8):1031–1042.

[Stampfli and Borel, 2002] Stampfli, G. M. and Borel, G. D. (2002). A plate tectonic model for the paleozoic and mesozoic constrained by dynamic plate boundaries and restored synthetic oceanic isochrons. *Earth and Planetary Science Letters*, 196(1-2):17–33.

[Stampfli and Borel, 2004] Stampfli, G. M. and Borel, G. D. (2004). The transmed transects in space and time: constraints on the paleotectonic evolution of the mediterranean domain. In Cavazza, W., Roure, F., Spakman, W., Stampfli, G. M., and Ziegler, P. A., editors, *The TRANSMED Atlas – The Mediterranean Region from Crust to Mantle*, pages 53–80. Springer, Berlin, Heidelberg.

[Theyer, 2022] Theyer, M. (2022). Porosity and permeability of the main lithologies of the kuhschneeberg. Master's thesis, University of Vienna, Vienna, Austria.

[Tollmann, 1985] Tollmann, A. (1985). *Geologie von Österreich, Band 2*. Franz Deuticke Wien, Vienna.

[Vasvari, 2001] Vasvari, V. (2001). *Geohydraulische und bohrlochgeophysikalische Untersuchungen in geklüfteten Grundwasserleitern*, volume 38 of *Schriftenreihe zur Wasserwirtschaft*. Schriftenreihe zur Wasserwirtschaft.

[Vinci Technologies, 2013] Vinci Technologies (2013). *COREVAL 700 - Unsteady state gas permeameter and porosimeter at overburden pressure: Operating Manual*. France, rev 01.1 edition. Operating manual.

[Webmineral.com,] Webmineral.com. Dolomite mineral data. https://webmineral.com/data/Dolomite.shtml. Accessed: 2025-03-20.

[Wessely, 1993] Wessely, G. (1993). Der untergrund des wiener beckens. In OMV, editor, *Erdöl und Erdgas in Österreich*. Veröffentlichungen aus dem Naturhistorischen Museum in Wien, Vienna.

[Wessely, 2006] Wessely, G. (2006). *Geologie der österreichischen Bundesländer NÖ*. Geologische Bundesanstalt, Wien.

10 Appendix

No.	E(M34)	N(M34)	FDC	Immersion method		Slug test	Coreval 700 [400 psi]	
				Raw density [g/cm³]	Porosity [%]	Permeability [mD]	Porosity [gas][%]	Klinkenberg permeability [mD]
L1/5	736758	318945	3	2.77	2.25	na	na	na
L1/9	736754	318941	3	2.78	1.24	na	na	na
L1/10	736753	318942	3	2.7	2	na	na	na
L6/1	736972	318673	2	2.78	2.16	na	na	na
L6/10	736962	318664	2	2.78	1.49	na	na	na
L8/2	736724	318920	3	2.79	1.54	na	na	na
L9/1	737131	318364	3	2.79	1.22	na	na	na
L11	737212	318336	2	2.76	2.43	na	na	na
L13	737345	318522	2	2.8	1.7	na	0.82	0.047
LK-MS5	736758	318945	3	2.8	1.22	0.08	0.78	1.601
LK-MS7	736753	318941	3	2.78	1.56	0.02	1.302	0.042
LK-MS8	736724	318920	1	2.81	0.33	0.09	1.815	0.618
LK-MS11	736695	318894	1	2.79	0.97	0.1	1.082	0.103
LK-MS12	736688	318891	2	2.8	1.02	2.1	1.063	0.986
LK-MS15	736678	318884	3	2.8	0.94	2.2	na	na
LK-MS18	736660	318821	2	2.74	2.27	0.08	1.308	0.009
LK-MS19	736671	318813	2	2.79	1.11	0.32	1.09	0.229
LK-MS20	736680	318810	2	2.77	1.67	0.09	1.99	0.08
LK-MS22	736757	318783	2	2.8	0.84	0.07	2.707	5.239
LK-MS24	736755	318775	2	2.77	0.8	0.03	3.375	0.117
LK-MS25	736752	318766	2	2.76	0.68	0.13	1.92	2.094
LK-MS29	737218	318338	3	2.79	1.24	2.6	2.065	0.006
LK-MS30	737222	318346	3	2.8	1.17	2	1.092	0.003
LK-MS31	737226	318354	3	2.77	1.3	0.23	1.702	0.002
LK-MS32	737272	318424	2	2.77	1.45	0.17	1.564	0.018
LK-MS33	737272	318436	2	2.76	1.81	0.56	1.534	0.009

Log	Thickness	Lithology	FDC	Direction	Dip	WPS89 E	WPS89 N	Comment	Avg Dir	Avg Dip
L1-1	140	Dol	2	92	40	16154753	48008946	Top	91	38
L1-2	35	Dol	3	92	40					
L1-3	60	Dol	3	92	30					
L1-4	165	Dol	3	95	41					
L1-5	150	Dol	3	95	41					
L1-6	60	Dol	3							
L1-7	95	Dol	3							
L1-8	190	Dol	3	97	41					
L1-9	80	Dol	3							
L1-10	100	Dol	3							
L1-11	20	Dol	2	75	33					
L1-12	145	Dol	3							
L1-13	160	Dol	3					Bottom		
GAP										
L2-1	80	Dol	3	47	33	16154211	48008830	Top	79	42
L2-2	55	Dol	3	68	32					
L2-3	170	Dol	4	61	24					
L2-4	120	Dol	3	61	30					
L2-5	210	Dol	2	48	30					
L2-6	30	Dol	3	111	33					
L2-7	30	Dol	2	111	37					
L2-8	150	Dol	2	117	35					
L2-9	200	Dol	1	102	42					
L2-10	85	Dol	2	33	56					
L2-11	300	Dol	1	91	54					
L2-12	80	Dol	2	104	45					
L2-13	30	Dol	3	98	45					
L2-14	160	Dol	2	98	40					
L2-15	70	Dol	2	118	42					
L2-16	40	Dol	2	118	42					
L2-17	350	Dol	2							
GAP	400	Dol								
L2-18	400	Dol	3							
L2-19	220	Dol	1							
L2-20	290	Dol	2	11	58					
L2-21	250	Dol	3	18	80			Bottom		
GAP										
L3-1	160	Dol	3	120	48	16153360	40008027	Bottom	126	47
L3-2	330	Dol	3	120	48					
L3-3		Dol	4					Unconformity		
L3-4	170	Dol	3	92	48					
L3-5	100	Dol	3	171	45			Top		
L4-1	220	Dol	4	128	58	16153928	48007910	Bottom	119	51
L4-2	110	Dol	3	128	58					
FAULT1		Dol		283	44			Fault Breccia		
L4-3	100	Dol	2	121	61					
L4-4	220	Dol	4	140	54					
L4-5	210	Dol	2	120	50					
L4-6	230	Dol	2							
L4-7	600	Dol	3							
L4-8	30	Dol	2	110	44					
L4-9	40	Dol	2	108	43					
L4-10	30	Dol	2	110	43					
L4-11	70	Dol	2	110	44	16154435	48007688	Top		
L5-1	55	Dol	3	160	35	16154592	48007687	Bottom	115	43
L5-2	210	Dol	2	112	50					
L5-3	30	Dol	3	123	50					
L5-4	40	Dol	3	123	50					
L5-5	100	Dol	3	123	50					
L5-6	60	Dol	2	107	48					
L5-7	250	Dol	2					Top		
L5-8	80	Dol	3	107	36					
L5-9	60	Dol	3	88	34					
L5-10	200	Dol	3	88	34	16157522	48006437	Bottom		
L6-1	90	Dol	2	110	42	16157562	48005325	Top	113	48
L6-2	40	Dol	2	113	38					
L6-3	40	Dol	2	119	51					

L6-4	40	Dol	2	108	60			Bottom		
L7-1	20	Dol	3	97	42			Top	104	39
L7-2	15	Dol	3	113	36					
L7-3	20	Dol	3	113	36					
L7-4	20	Dol	4	92	40			Bottom		
L8-1	75	Dol	3	140	50			Top	107	44
L8-2	18	Dol	3	102	42					
L8-3	19	Dol	3	102	42					
L8-4	32	Dol	3	90	40					
L8-5	35	Dol	3	105	46					
L8-6	110	Dol	3	105	46			Bottom		
L9-1	100	Dol	3	82	42			Bottom	91	46
L9-2	80	Dol	3	100	50			Top		
L10-1	30	Dol	2	88	45			Bottom	85	44
L10-2	30	Dol	3	98	54					
L10-3	55	Dol	3	100	42					
L10-4	90	Dol	3	70	40					
L10-5	30	Dol	3	70	38			Top		
L11-1	90	Dol	2	92	35			Bottom	92	34
L11-2	110	Dol	2	92	35					
L11-3	20	Dol	2	92	35					
L11-4	20	Dol	2	92	35					
L11-5	85	Dol	2	90	46					
L11-6	160	Dol	2	90	46					
L11-7	25	Dol	3	95	20					
L11-8	70	Dol	3	95	20			Top		
L12-1	500	Dol	3	92	62			Bottom	92	62
L12-2	400	Dol	3					Top		
L13-1	400	Dol	2	104	38			Bottom	101	36
L13-2	20	Dol	3	98	34					
L13-3	160	Dol	2					Top		

No	Name	Pc(psi)	K[n2](mD)	K∞(mD)	Vp(cc)	b[n2](psi)	Vp0(cc)	Vp0(%)	Vp(%)	β(ft^{-1})	α(μm)	Gas	Vg(cc)	ρg (g/cc)	ρb (g/cc)	Date	Time	ρb0 (g/cc)	Operator	Depth	Length(mm)	Diameter(mm)	Weight(g)
0	LK8	400	0.956939	0.618653	0.849081	8.202157	1.227485	2.603761	1.815657	8.98E+10	188.206	N2	45.91531	2.84726408	2.795568	26/03/2025 16:20	16:20:23	2.773128	Vinci Tech	0	41.45199203	37.90006716	130.733002
1	LK8	500	0.899465	0.576219	0.820172	8.414682	1.227485	2.603761	1.754924	1.32E+11	258.3874	N2	45.91531	2.84726408	2.797297	26/03/2025 16:29	16:29:56	2.773128	Vinci Tech	0	41.43285751	37.89709868	130.733002
2	LK8	1000	0.565734	0.336592	0.694642	10.21155	1.227485	2.603761	1.490331	5.39E+10	67.3914	N2	45.91531	2.84726408	2.80483	26/03/2025 16:56	16:56:40	2.773128	Vinci Tech	0	41.35769653	37.88054332	130.733002
3	LK8	1500	0.398225	0.222442	0.625297	11.85362	1.227485	2.603761	1.343552	6.53E+08	0.5906	N2	45.91531	2.84726408	2.80901	26/03/2025 17:08	17:08:10	2.773128	Vinci Tech	0	41.28499985	37.88566541	130.733002
4	LK8	2500	0.232151	0.116165	0.507162	14.97691	1.227485	2.603761	1.092493	2.19E+11	116.3229	N2	45.91531	2.84726408	2.816158	26/03/2025 17:21	17:21:00	2.773128	Vinci Tech	0	41.20614243	37.87374004	130.733002
5	LK8	3500	0.148581	0.067015	0.427549	18.25692	1.227485	2.603761	0.922578	3.21E+11	110.722	N2	45.91531	2.84726408	2.820996	26/03/2025 17:37	17:37:41	2.773128	Vinci Tech	0	41.14418793	37.86972974	130.733002
6	LK8	4500	0.099813	0.040614	0.355754	21.86372	1.227485	2.603761	0.768847	3.30E+11	77.94216	N2	45.91531	2.84726408	2.825373	26/03/2025 18:04	18:04:09	2.773128	Vinci Tech	0	41.07141113	37.87389502	130.733002
7	LK8	5500	0.068359	0.024983	0.304262	26.04342	1.227485	2.603761	0.658297	7.81E+10	12.89913	N2	45.91531	2.84726408	2.828521	26/03/2025 18:37	18:37:04	2.773128	Vinci Tech	0	41.0271759	37.87321639	130.733002
8	LK8	6500	0.043748	0.013918	0.268027	32.14827	1.227485	2.603761	0.580354	3.96E+12	471.0358	N2	45.91531	2.84726408	2.83074	26/03/2025 19:19	19:19:06	2.773128	Vinci Tech	0	40.95549393	37.89148364	130.733002
9	LK5	400	2.222796	1.601092	0.494769	5.824508	1.247842	1.945104	0.780395	1.73E+11	935.2593	N2	62.90512	2.84668397	2.824469	01/04/2025 15:39	15:39:09	2.791313	Vinci Tech	0	56.29401398	37.8676369	179.070999
10	LK5	500	2.00406	1.426611	0.466653	6.071543	1.247842	1.945104	0.736374	2.01E+11	970.3658	N2	62.90512	2.84668397	2.825722	01/04/2025 15:55	15:55:35	2.791313	Vinci Tech	0	56.26750946	37.868155	179.070999
11	LK5	1000	1.586356	1.097994	0.455294	6.671647	1.247842	1.945104	0.718578	2.83E+11	1047.865	N2	62.90512	2.84668397	2.826228	01/04/2025 16:05	16:05:42	2.791313	Vinci Tech	0	56.22851944	37.87788671	179.070999
12	LK5	1500	1.235843	0.82814	0.411243	7.384681	1.247842	1.945104	0.649505	3.86E+11	1121.968	N2	62.90512	2.84668397	2.828195	01/04/2025 16:14	16:14:05	2.791313	Vinci Tech	0	56.17942429	37.88125853	179.070999
13	LK5	2500	0.827848	0.523758	0.357176	8.708875	1.247842	1.945104	0.564595	5.43E+11	972.6388	N2	62.90512	2.84668397	2.830612	01/04/2025 16:23	16:23:55	2.791313	Vinci Tech	0	56.1309433	37.88143015	179.070999
14	LK5	3500	0.59111	0.354317	0.319735	10.02462	1.247842	1.945104	0.505711	6.06E+11	741.721	N2	62.90512	2.84668397	2.832288	01/04/2025 16:34	16:34:54	2.791313	Vinci Tech	0	56.09212494	37.88332049	179.070999
15	LK5	4500	0.444189	0.25321	0.28979	11.31348	1.247842	1.945104	0.458566	4.16E+11	367.0965	N2	62.90512	2.84668397	2.83363	01/04/2025 16:47	16:47:18	2.791313	Vinci Tech	0	56.05391693	37.88725412	179.070999
16	LK5	5500	0.341348	0.18508	0.262751	12.66483	1.247842	1.945104	0.415957	1.51E+11	102.4252	N2	62.90512	2.84668397	2.834843	01/04/2025 17:01	17:01:31	2.791313	Vinci Tech	0	56.015522	37.89212747	179.070999
17	LK7	400	0.103476	0.042517	0.586864	21.50639	1.250113	2.73442	1.302566	1.95E+11	38.39251	N2	44.46756	2.84620952	2.809136	21/05/2025 09:51	09:51:12	2.768382	Vinci Tech	0	40.36727524	37.69719869	126.564003
18	LK5	6500	0.266299	0.137248	0.240003	14.10416	1.247842	1.945104	0.380082	1.47E+11	81.9244	N2	62.90512	2.84668397	2.835864	01/04/2025 17:18	17:18:04	2.791313	Vinci Tech	0	55.98480988	37.89569411	179.070999
19	LK11	400	0.211271	0.103527	0.544457	15.61096	1.19835	2.351452	1.082243	9.88E+10	42.65884	N2	49.76375	2.84373653	2.81296	21/05/2025 10:32	10:32:39	2.776867	Vinci Tech	0	44.81917572	37.8044179	141.514999
20	LK18	400	0.032413	0.009326	0.751595	37.13274	1.26071	2.175481	1.308447	2.11E+13	1439.207	N2	56.69016	2.83634785	2.799236	21/05/2025 11:14	11:14:09	2.774644	Vinci Tech	0	50.89690399	37.90733095	160.792999
21	LK19	400	0.409442	0.229907	0.919118	11.7136	1.766763	2.07591	1.090809	1.24E+11	100.1362	N2	83.34109	2.85127077	2.820169	21/05/2025 13:16	13:16:09	2.792081	Vinci Tech	0	74.66995239	37.90472744	237.628006
22	LK20	400	0.171743	0.080224	0.885128	17.11194	1.268228	2.827634	1.990479	1.14E+12	337.9805	N2	43.58298	2.84849729	2.791799	21/05/2025 13:50	13:50:09	2.767952	Vinci Tech	0	39.58254242	37.82052463	124.146004
23	LK22	400	6.56696	5.239285	1.07531	3.801116	1.201592	3.015574	2.707231	1.24E+10	214.4378	N2	38.64462	2.84642505	2.769366	21/05/2025 14:21	14:21:48	2.760589	Vinci Tech	0	35.33593369	37.83127561	109.999001
24	LK24	400	0.234862	0.11782	1.009797	14.9008	1.429419	4.711671	3.37519	3.36E+11	144.1576	N2	28.90842	2.84252787	2.746587	21/05/2025 15:29	15:29:38	2.708597	Vinci Tech	0	26.69655037	37.77420692	82.1729965
25	LK25	400	2.832476	2.094213	0.887532	5.28788	1.456587	3.113073	1.92022	3.78E+10	265.5413	N2	45.33278	2.8436378	2.789034	21/05/2025 16:00	16:00:46	2.755113	Vinci Tech	0	41.14378738	37.81981121	128.910004
26	LK12	400	1.442619	0.98658	0.632225	6.933644	1.687859	2.789108	1.06327	1.47E+11	487.6472	N2	58.82821	2.84280266	2.812576	02/04/2025 12:48	12:48:41	2.763514	Vinci Tech	0	52.80167007	37.86563822	167.237
27	LK12	500	1.274855	0.85785	0.657099	7.29157	1.687859	2.789108	1.10464	1.72E+11	498.0598	N2	58.82821	2.84280266	2.8114	02/04/2025 13:15	13:15:19	2.763514	Vinci Tech	0	52.80167007	37.87355742	167.237
28	LK12	1000	0.815206	0.514549	0.556758	8.764666	1.687859	2.789108	0.93754	1.23E+11	215.31	N2	58.82821	2.84280266	2.81615	02/04/2025 13:53	13:53:29	2.763514	Vinci Tech	0	52.74542999	37.86177005	167.237
29	LK12	1500	0.553286	0.327934	0.464846	10.3078	1.687859	2.789108	0.78398	5.29E+10	62.19941	N2	58.82821	2.84280266	2.820516	02/04/2025 14:14	14:14:55	2.763514	Vinci Tech	0	52.74837875	37.83140121	167.237
30	LK12	2500	0.304321	0.161249	0.378518	13.30915	1.687859	2.789108	0.639317	2.33E+11	161.6623	N2	58.82821	2.84280266	2.824628	02/04/2025 14:52	14:52:15	2.763514	Vinci Tech	0	52.6832962	37.82719442	167.237
31	LK12	3500	0.194205	0.093359	0.37462	16.20291	2.371912	3.875665	0.632774	3.44E+11	154.5194	N2	58.82821	2.84280266	2.824814	02/04/2025 15:22	15:22:34	2.732625	Vinci Tech	0	NaN	37.47313678	167.237
32	LK12	4500	0.141362	0.062977	0.380062	18.66996	2.371912	3.875665	0.641906	9.84E+11	330.6483	N2	58.82821	2.84280266	2.824555	02/04/2025 15:50	15:50:37	2.732625	Vinci Tech	0	NaN	37.47485886	167.237
33	LK12	5500	0.107798	0.044781	0.362419	21.10837	2.371912	3.875665	0.612291	1.72E+11	42.92847	N2	58.82821	2.84280266	2.825396	02/04/2025 16:21	16:21:28	2.732625	Vinci Tech	0	NaN	37.46927519	167.237
34	LK31	400	0.002722	2.79E-04	0.964396	131.3572	1.635944	2.854433	1.70265	1.59E+15	6836.476	N2	55.67647	2.84292454	2.794519	22/05/2025 08:56	08:56:04	2.761775	Vinci Tech	0	50.42485046	37.81792379	158.283997
35	LK25	500	2.096388	1.50008	0.847781	5.962768	1.448885	3.096612	1.835489	4.69E+10	226.0024	N2	45.34048	2.84315476	2.790969	22/05/2025 10:12	10:12:01	2.755113	Vinci Tech	0	41.13474655	37.8108512	128.910004
36	LK25	1000	1.293828	0.872331	0.750765	7.24776	1.448885	3.096612	1.628868	8.93E+10	262.3607	N2	45.34048	2.84315476	2.796844	22/05/2025 10:21	10:21:55	2.755113	Vinci Tech	0	41.08072662	37.79594658	128.910004
37	LK25	1500	0.901192	0.57749	0.685763	8.40801	1.448885	3.096612	1.489938	8.79E+10	172.1407	N2	45.34048	2.84315476	2.800793	22/05/2025 10:30	10:30:18	2.755113	Vinci Tech	0	41.04589462	37.78530759	128.910004
38	LK12	6500	0.083279	0.032227	0.346288	23.7625	2.371912	3.875665	0.585198	8.56E+11	165.9528	N2	58.82821	2.84280266	2.826167	02/04/2025 16:58	16:58:04	2.732625	Vinci Tech	0	NaN	37.46416922	167.237
39	LK25	3500	0.347842	0.189303	0.549754	12.56241	1.448885	3.096612	1.197977	1.69E+10	11.72128	N2	45.34048	2.84315476	2.809094	22/05/2025 10:41	10:41:31	2.755113	Vinci Tech	0	40.93999863	37.77820245	128.910004
40	LK25	4500	0.239137	0.120438	0.508171	14.7834	1.448885	3.096612	1.108367	1.68E+10	8.578271	N2	45.34048	2.84315476	2.811642	22/05/2025 10:55	10:55:59	2.755113	Vinci Tech	0	40.90931702	37.77523988	128.910004
41	LK25	5500	0.181179	0.085706	0.474058	16.70959	1.448885	3.096612	1.034732	2.74E+11	102.2051	N2	45.34048	2.84315476	2.813736	22/05/2025 11:12	11:12:53	2.755113	Vinci Tech	0	40.86992645	37.7793767	128.910004
42	LK25	6500	0.133967	0.058882	0.448244	19.12733	1.448885	3.096612	0.978939	3.48E+11	99.60146	N2	45.34048	2.84315476	2.815322	22/05/2025 11:33	11:33:11	2.755113	Vinci Tech	0	40.82744598	37.78837588	128.910004
43	LK24	500	0.181447	0.085862	0.924259	16.69864	1.445571	4.76491	3.099819	4.37E+11	122.9941	N2	28.89227	2.84411691	2.755954	22/05/2025 12:14	12:14:09	2.708597	Vinci Tech	0	26.68622398	37.71725193	82.1729965
44	LK22	500	Infinity	NaN	1.039571	NaN	1.215447	3.050345	2.620525	0	NaN	N2	38.63076	2.84747179	2.772853	22/05/2025 13:43	13:43:35	2.760614	Vinci Tech	0	35.31540298	37.81863844	110
45	LK22	1000	Infinity	NaN	0.919991	NaN	1.215447	3.050345	2.326104	0	NaN	N2	38.63076	2.84747179	2.781237	22/05/2025 13:51	13:51:31	2.760614	Vinci Tech	0	35.2395668	37.80220644	110
46	LK22	1500	Infinity	NaN	0.837265	NaN	1.215447	3.050345	2.121375	0	NaN	N2	38.63076	2.84747179	2.787066	22/05/2025 13:58	13:58:53	2.760614	Vinci Tech	0	35.16872406	37.80066586	110
47	LK22	500	2.703018	1.988766	0.949091	5.387148	1.215447	3.050345	2.397914	1.37E+09	10.93175	N2	38.63076	2.84747179	2.779192	22/05/2025 14:14	14:14:01	2.760614	Vinci Tech	0	35.30548096	37.78079311	110
48	LK22	1500	2.005046	1.427395	0.790645	6.070343	1.215447	3.050345	2.005624	1.75E+10	99.74343	N2	38.63076	2.84747179	2.790362	22/05/2025 14:45	14:45:53	2.760614	Vinci Tech	0	35.17132568	37.77693689	110
49	LK22	2500	1.626468	1.129253	0.697756	6.604566	1.215447	3.050345	1.774172	2.09E+10	98.28128	N2	38.63076	2.84747179	2.796953	22/05/2025 19:24	19:24:01	2.760614	Vinci Tech	0	35.08971786	37.77625482	110
50	LK29	400	0.022703	0.005754	0.988152	44.18373	1.70855	3.518683	2.065702	9.67E+13	3678.462	N2	46.84796	2.85293135	2.793998	03/04/2025 10:30	10:30:52	2.752546	Vinci Tech	0	NaN	37.81631117	133.654007
51	LK22	3500	1.658321	1.154125	0.620273	6.552968	1.215447	3.050345	1.580271	1.95E+10	73.26857	N2	38.63076	2.84747179	2.802474	23/05/2025 00:57	00:57:35	2.760614	Vinci Tech	0	35.03374863	37.76915774	110
52	LK30	400	0.01576	0.003479	0.869264	52.95923	1.827152	2.270023	1.092965	1.53E+14	2775.527	N2	78.66332	2.85317217	2.821988	03/04/2025 12:37	12:37:45	2.788405	Vinci Tech	0	70.60619354	37.87095109	224.440002
53	LK22	4500	1.355124	0.919255	0.563681	7.112335	1.215447	3.050345	1.438165	2.57E+10	76.67839	N2	38.63076	2.84747179	2.80652	23/05/2025 08:15	08:15:51	2.760614	Vinci Tech	0	34.96197891	37.78063843	110
54	LK19	500	Infinity	NaN	0.798726	NaN	1.769532	2.079164	0.949316	0	NaN	N2	83.33832	2.85136552	2.824297	23/05/2025 09:18	09:18:45	2.792081	Vinci Tech	0	74.64226532	37.88403937	237.628006
55	LK19	1500	Infinity	NaN	0.713134	NaN	1.769532	2.079164	0.848449	0	NaN	N2	83.33832	2.85136552	2.827173	23/05/2025 09:31	09:31:46	2.792081	Vinci Tech	0	74.56819153	37.88356688	237.628006
56	LK32	400	0.053943	0.018346	1.035347	29.10559	1.761105	2.63287	1.564832	1.57E+13	1486.399	N2	65.12807	2.84193871	2.797467	03/04/2025 15:50	15:50:21	2.767114	Vinci Tech	0	58.69586945	37.88438714	185.089996
57	LK13	400	0.113668	0.047888	0.456413	20.60483	1.084425	1.927404	0.820362	2.15E+12	479.4495	N2	55.1791	2.84190926	2.818595	03/04/2025 09:23	09:23:28	2.787134	Vinci Tech	0	49.44708252	37.84955433	156.813995
58	LK33	400	0.03166	0.009036	0.604051	37.55774	1.034813	2.600737	1.534742	2.48E+13	1384.467	N2	38.75439	2.84045239	2.796859	04/04/2025 09:36	09:36:20	2.76658	Vinci Tech	0	35.03693771	37.81907783	110.080002